THE ROLE OF SHEAR AND TENSILE FAILURE IN DYNAMICALLY TRIGGERED LANDSLIDES

by
Tamara L. Gipprich

A thesis submitted to the Faculty and the Board of Trustees of the Colorado School of Mines in partial fulfillment of the requirements for the degree of Master of Science (Geophysics).

Golden, Colorado

Date _____

Signed: _____
Tamara L. Gipprich

Approved: _____
Dr. Roelof K. Snieder
Professor of Geophysics
Thesis Advisor

Golden, Colorado

Date _____

_____
Dr. Terence K. Young
Professor and Head,
Department of Geophysics

ABSTRACT

The dynamic stress generated by earthquakes is one of the significant causes for triggering landslides. Many methods characterize the triggering of landslides, but the role of dynamic effects which produce slope instability is not fully understood. Current methods, such as pseudostatic analysis and Newmark's method, focus on earthquake accelerations to monitor landslide potential. These methods depend on shear failure to analyze instability, so the role of tensile failure is not clear.

We develop a limit-equilibrium model to investigate the dynamic stress generated from a given ground motion and show how this can be used to assess the role of shear and tensile failure in the initiation of slope instability. This method monitors how compressive and extensional stress components created from a plane P- or S-wave produce failure. This is done by incorporating the modified Griffith failure envelope (Brace, 1960), which has the feature of combining shear and tensile failure in a single criterion, while the Mohr-Coulomb theory accounts for shear failure only. Tests of dynamic stress in both homogeneous and layered slopes demonstrate that two modes of failure exist. This analysis provides examples of tensile failure in the upper meters of a slope due to the $\sigma_{xx}^{dynamic}$ component of stress, while shear failure takes place at greater depth. Further, we derive dynamic stress equations, independent of the dynamic stress produced in the model, which give the dynamic stress in the near-surface when the ground motion at the surface is known. These equations are used to approximately define the depth for each mechanism of failure in a slope. From this information, we assess that shear and tensile failure ultimately collaborate in the formation of landslides.

In addition, we investigate slope instability for deep-water environments when pore-fluid pressure is introduced into a slope. Overpressure is a damaging phenomenon which can cause submarine slope failure and extensive costs to the exploration industry. This model is a useful tool for understanding the stress involved in deep-water sediments and the stability of submarine slopes.

This project provides an additional viewpoint about the manner in which particular earthquakes cause slope failure. An understanding of shear and tensile failure in triggered slopes can help to create a more complete dynamic model.

TABLE OF CONTENTS

LIST OF FIGURES

LIST OF TABLES

ACKNOWLEDGEMENTS

My sincere appreciation is given to my advisor Dr. Roel Snieder. You have helped me to expand my personal and academic goals and to fully realize my interest for geophysical hazards. Not only did your guidance and teaching enhance my experience as a graduate student, but I will always remember your advice on transitioning through life.

Additionally, I would like to thank visiting student Wouter Kimman from Utrecht University and each of my graduate committee members: Dr. Terry Young and Dr. Vaughan Griffiths of the Colorado School of Mines and Dr. Randall Jibson and Dr. David Wald of the U. S. Geological Survey. Each has provided their own expertise in hazard studies to help make this project a success. I greatly appreciate the financial support provided by the National Earthquake Hazards Reduction Program (NEHRP), which has sponsored this research, award #04HQGR0108.

I would also like to extend my thanks to Dr. Matthew Haney for his enlightening discussions and for providing numerical code to aid in the interest of this project.

Finally, I express my gratitude to my family and friends, who have supported me throughout this process and who have been a source of encouragement when I needed it most.

Chapter 1

INTRODUCTION

The term *natural hazard* implies a natural phenomenon which may cause direct damage, injury, and harm to those in its path (Selby, 1993). Among the many types of hazards, seismically triggered landslides have the potential to cause devastation to life and property. This hazard has greatly increased because of the expansion of commercial and residential development into earthquake-prone slopeside locations. Even 20 years ago, it was estimated that all landslide hazards annually cause as much as $2 billion in damage and as many as 50 deaths within the United States alone (Committee on Ground Failure, 1985).

Most moderate and large earthquakes produce ground motions that can trigger landslides, which poses a double threat to those living in these risk areas: the earthquake itself and the subsequent triggered landslide. In January 2001, an earthquake of magnitude 7.7 shook El Salvador and triggered a devastating landslide in the town of Santa Tecla (Figure 1.1). The landslide destroyed more than 300 homes and caused about 750 deaths (Evans & Bent, 2004; Konagai *et al.*, 2004). This is why this type of hazard calls attention to the scientific community the need to help understand the triggering mechanism of landslides.

1.1 Current Methods Used to Characterize Triggered Landslides

Several methods have been established to understand how earthquake-triggered landslides behave, but the role of dynamic effects that produce slope instability is not

Figure 1.1. Landslide triggered by the 2001 El Salvador earthquake (from Jibson & Crone, 2001).

fully understood. Two methods are commonly used to model earthquake-triggered landslides: pseudostatic analysis and Newmark's method.

Pseudostatic analysis was developed in the 1940's as a way to account for the effect of earthquakes on earth dams (Terzaghi *et al.*, 1996). This is a limit-equilibrium analysis where the acceleration due to an earthquake is computed as an additional static body force on the slope. A factor of safety (FS) analysis is carried out for different acceleration values to determine which critical value brings the slope to failure, reducing the factor of safety to 1.0 (Jibson, 1993). The factor of safety gives the stability of a slope as the ratio of resisting to driving forces. When this ratio is greater than 1.0, the slope is stable. When less than 1.0, the slope begins to move (Jibson *et al.*, 2000). This method accounts for the accelerations a slope can tolerate without deforming. Because it is a limit-equilibrium analysis, however, it tells the user nothing about what will occur once the yield acceleration is exceeded (Jibson, 1993).

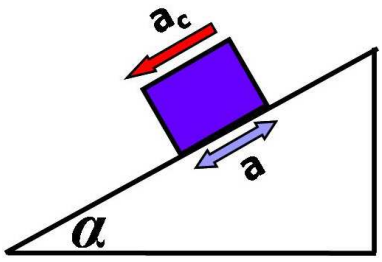

Figure 1.2. Motion of a sliding block once critical acceleration, a_c, is surpassed during an earthquake using Newmark's method of analysis. Newmark's method calculates the total displacement of the landslide from acceleration-time histories of an earthquake (modified from Jibson *et al.*, 2000).

Newmark's method (Newmark, 1965) goes further by estimating the permanent slope displacement caused by an earthquake. Equation (1.1) provides the critical acceleration a slope can withstand during an earthquake and is calculated by using the static factor of safety and slope geometry (Jibson *et al.*, 2000)

$$a_c = (FS - 1)g\sin(\alpha)\ , \tag{1.1}$$

where g is gravitational acceleration and α can be estimated as the slope angle.

An acceleration larger than this value during an earthquake initiates sliding on a slope (Figure 1.2) (Jibson, 1993). The block shown in this figure represents any type of soil or sediment resting at the surface. Newmark's method is used to calculate the permanent displacement of the slope by integrating an earthquake acceleration-time history twice over the times that exceed the critical acceleration (Jibson, 1993; Jibson *et al.*, 2000). Newmark's method is most reliable when accurate data of the slope geometry, soil strength properties, and earthquake acceleration are known (Jibson *et al.*, 2000). In this analysis, all slopes having the same critical acceleration produce

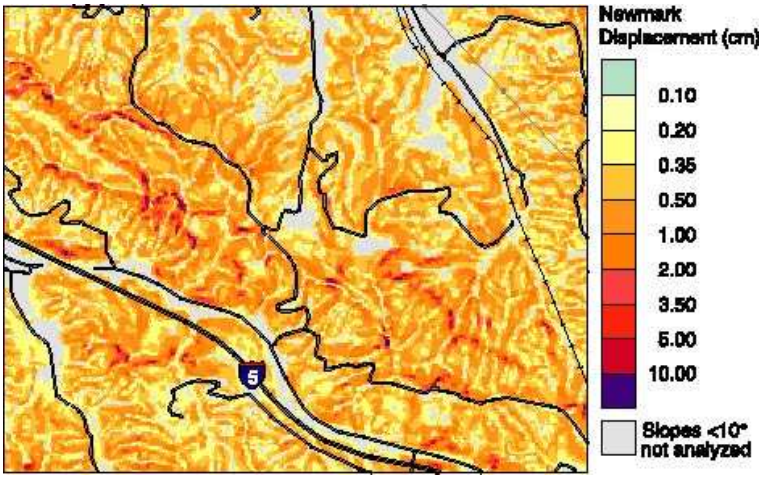

Figure 1.3. Map of predicted Newmark displacements for a portion of the Oat Mountain quadrangle for the 1994 Northridge, California earthquake (from Jibson *et al.*, 2000).

the same Newmark displacement for a given strong motion record. Thus, the displacement depends ultimately on the critical acceleration regardless of differences in geometry and physical properties of a slope (Jibson *et al.*, 2000).

As shown by Jibson *et al.* (2000), Newmark's analysis can be used in geographic information system (GIS) software to create landslide hazard maps for slopes susceptible to sliding during an earthquake. This is done by assigning strength data to each geological unit and creating a slope map from a digital elevation model (DEM) for any given location. By combining this information in GIS, the factor of safety can be calculated for each cell. Critical acceleration is displayed in map format by combining the FS and slope data to show locations that will fail when a certain acceleration is surpassed. These data along with knowledge of the shaking intensity for a particular earthquake are then used to estimate the Newmark displacement. An example of a Newmark displacement map is shown in Figure 1.3, produced with data calculated

Figure 1.4. Photograph taken after the Northridge, CA earthquake in 1994 showing extensional cracks caused by the dynamic stress of the earthquake (from Randall Jibson, U.S. Geological Survey)

.

from the Northridge, California earthquake of 1994 (Jibson *et al.*, 2000).

1.2 Motivation for this Project

The project outlined in this paper follows a limit-equilibrium analysis for dynamic failure. While the previous two methods focus on earthquake accelerations to account for shear failure, this project concentrates on dynamic stress generated from a given ground motion and how this causes both shear and tensile failure at the initiation of slope instability. Post-failure deformation of a slope is not analyzed with this method. The image shown in Figure 1.4 taken after the Northridge, California earthquake in 1994, shows an example of extensional failure. Tensile cracks formed at the surface due to the additional dynamic stress imposed from the earthquake. This type of failure mechanism is modeled in this study.

The following chapters outline the use of this method and determine the role of

shear and tensile failure within a slope. In Chapter 2, the stress model created to analyze static and dynamic stress for a dry, infinite slope is described. By testing several wave propagation scenarios, we show in Chapter 3 that two modes of failure take place in a homogeneous slope. This analysis shows that tensile failure, due to dynamic stress, occurs in the near surface of a slope, while shear failure takes place at greater depth. Similarly, in Chapter 4, tests conducted on a realistic, layered slope are shown, where the shallow surface represents a weathered layer with low velocity. In Chapter 5, we focus on slope failure in a deep marine environment where pore-fluid pressure is introduced into the slope model. Overpressure is a damaging phenomena causing submarine slope failure and major costs for the energy exploration industry. This model is a useful tool for understanding the stress involved in deep-water sediments and the stability of submarine slopes. Finally, we conclude by drawing together information from these chapters and demonstrate how shear and tensile failure mechanisms collaborate to create slope failure.

Chapter 2

STRESS IN A SLOPE AND EMPLOYED FAILURE CRITERIA

The model created for this project analyzes two main components of stress within a slope: static stress for a dry, infinite slope and dynamic stress from an incoming plane wave. Once both components are known, we conduct a failure analysis for a given slope.

2.1 Static Stress of a Slope

We first consider the static stress in a 2D infinite slope, following Terzaghi's effective stress principle for normal stress (Terzaghi *et al.*, 1996),

$$\sigma'_{ij} = \sigma_{ij} - P\delta_{ij} \ , \tag{2.1}$$

where δ_{ij} is the Kroncker delta and P, pore-fluid pressure. In Chapters 2-4, we assume unsaturated conditions, where the pore-fluid pressure, P, is zero in the slope. This means that the total normal stress, σ, is equal to the effective normal stress, σ'. In Chapter 5, pore-pressure is introduced to influence stress within a slope.

We employ a simple static stress model for near-surface stress caused by gravity (Savage & Swolfs, 1992). The coordinate system used throughout the project is shown in Figure 2.1 where the x-direction is parallel to the surface of the slope and depth, z, is normal to the surface. In this paper, the horizontal direction means parallel to the slope while the vertical direction is normal to the slope.

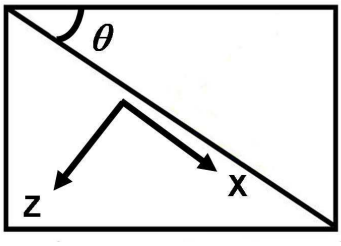

Figure 2.1. Coordinate system used throughout the model, where θ is the slope angle, the x-direction is parallel to the slope and the z-direction is normal to the slope.

For equilibrium to be maintained, a balance of forces must act on the slope. This is described by the derivation of static stress equations in Jaeger & Cook (1976) and Savage & Swolfs (1992), which are used for the basis of characterizing static stress in this project. The equations of equilibrium are partial differential equations describing how stress and displacement vary through the interior of the slope (Jaeger & Cook, 1976). In this model, the near surface is assumed to be linearly elastic, and the slope is laterally constrained so material cannot expand in the direction parallel to the slope. The slope is also approximated as an infinitely large, planar slope (Mello & Pratson, 1999). Because of lateral constraint in an infinite slope, stress does not depend on the horizontal location.

The governing equations of stress produced from these observations are given by:

$$\sigma_{xx}^{static} = \frac{\lambda}{\lambda + 2\mu} \rho g z \cos(\theta) \ , \tag{2.2}$$

$$\sigma_{zz}^{static} = \rho g z \cos(\theta) \ , \tag{2.3}$$

$$\sigma_{xz}^{static} = \rho g z \sin(\theta) \ , \tag{2.4}$$

where λ and μ are Lamé elastic constants, ρ is the density of the soil, g is gravitational

acceleration, and θ is the slope angle. Here, σ_{xx}^{static} and σ_{zz}^{static} are normal stress components acting in the x- and z-directions, respectively, while σ_{xz}^{static} is the shear stress acting in each of these directions. The sign convention used in this analysis is positive for compressive normal stress, and negative for tensile stress. The derivation of these stress components is in Appendix A.

The static stress in the vertical direction is related to horizontal stress since material expands in the horizontal under a vertical load. The constraint that expansion in the horizontal direction is not possible gives a horizontal stress, $\sigma_{xx}^{static} = (\lambda/(\lambda+2\mu))\sigma_{zz}^{static}$ (Selby, 1993). This can also be written as $\sigma_{xx}^{static} = (\nu/(1-\nu))\sigma_{zz}^{static}$, where ν is Poisson's ratio (e.g., Savage & Swolfs, 1992),

$$\frac{\lambda}{\lambda + 2\mu} = \frac{\nu}{1 - \nu} \, . \tag{2.5}$$

Poisson's ratio is defined as the ratio of strain in the direction of the load to the strain normal to the load. The value of this ratio commonly ranges between 0.2 and 0.4 and is normally described in terms of elastic parameters (Reid & Iverson, 1992),

$$\nu = \frac{\lambda}{2(\lambda + \mu)} \, . \tag{2.6}$$

2.2 Dynamic Stress for a Plane Wave Incident on a Slope

The dynamic stress created from a plane wave incident on a slope is computed using a 1D finite-element wave equation code (Haney, 2004). This incorporates second-order equations of motion that solve for displacement, u_x and u_z (Haney, 2004). Since we are interested in tensile failure, we limit ourselves to analyzing P-SV waves.

We consider the solutions of the form $F = (t - px, z)$ that describe a plane wave moving in the x-direction in time with a horizontal slowness, p. In a medium varying

with depth only, p is constant and known as the ray parameter of the incoming wave, given as (Aki & Richards, 2002)

$$p = \frac{\sin(i_p)}{v_p} = \frac{\sin(i_s)}{v_s} \ , \tag{2.7}$$

where i_p and i_s are the incidence angles that P- and S-waves make with the normal axis of the slope, and v_p and v_s are the P- and S-wave velocities, respectively. This solution expresses the x-derivative in terms of the time derivative

$$\frac{\partial F(t - px, z)}{\partial x} = -p \frac{\partial F(t - px, z)}{\partial t} \ . \tag{2.8}$$

The output of the code produces displacement, velocity, and acceleration as well as the stress components, $\sigma_{xx}^{dynamic}$, $\sigma_{zz}^{dynamic}$, and $\sigma_{xz}^{dynamic}$ from the incoming wave. At the free surface of the slope, the boundary conditions state that the tractions vanish, or that $\sigma_{zz}^{dynamic}(z = 0) = \sigma_{xz}^{dynamic}(z = 0) = 0$ (Aki & Richards, 2002).

Once dynamic stress is computed, the total stress state of the slope is formed by adding the dynamic and static components of stress for each location within the slope:

$$\sigma_{ij}^{total} = \sigma_{ij}^{static} + \sigma_{ij}^{dynamic} \ . \tag{2.9}$$

2.3 Principal Stress

To complete the failure analysis of a slope, the principal stresses must be calculated. The stress matrix for any particular location is given as:

$$\sigma_{ij} = \begin{bmatrix} \sigma_{xx} & \sigma_{xz} \\ \sigma_{zx} & \sigma_{zz} \end{bmatrix} \ , \tag{2.10}$$

where σ_{xz} is equal to σ_{zx} due to symmetry (Turcotte & Schubert, 2002). The eigenvalues of the stress matrix are the principal stress components, a maximum, σ_1, and minimum, σ_3 (Middleton & Wilcock, 1994). In two directions, the principal stress components are given by (Iverson & Reid, 1992):

$$\sigma_1 = \frac{\sigma_{xx} + \sigma_{zz}}{2} + \sqrt{\left(\frac{\sigma_{xx} - \sigma_{zz}}{2}\right)^2 + \sigma_{xz}^2}\,, \tag{2.11}$$

$$\sigma_3 = \frac{\sigma_{xx} + \sigma_{zz}}{2} - \sqrt{\left(\frac{\sigma_{xx} - \sigma_{zz}}{2}\right)^2 + \sigma_{xz}^2}\,. \tag{2.12}$$

The principal stress components represent normal stress acting on two orthogonal planes, where shear stress vanishes. The anticipated principal stress directions are given by the eigenvectors of the stress matrix (e.g., Middleton & Wilcock, 1994).

Figure 2.2 displays the static principal stress components for a slope of 26°. The directions of the arrows indicate principal stress directions while the length represents the magnitude of the principal stress component. Inward pointing arrows represent compressional stress. For a homogeneous medium, the weight of the sediments increases uniformly as shown by equations (2.2-2.4). This explains the increase of principal stress with depth (e.g., Mello & Pratson, 1999).

2.4 Determining Failure

Once a wave passes through a slope, additional dynamic stress is generated that may cause certain locations within the slope to fail. To understand the potential for these locations to fail, we address the behavior of the slope sediments under stress. For shear failure, this is commonly done using a Mohr-Coulomb failure analysis (Mello & Pratson, 1999).

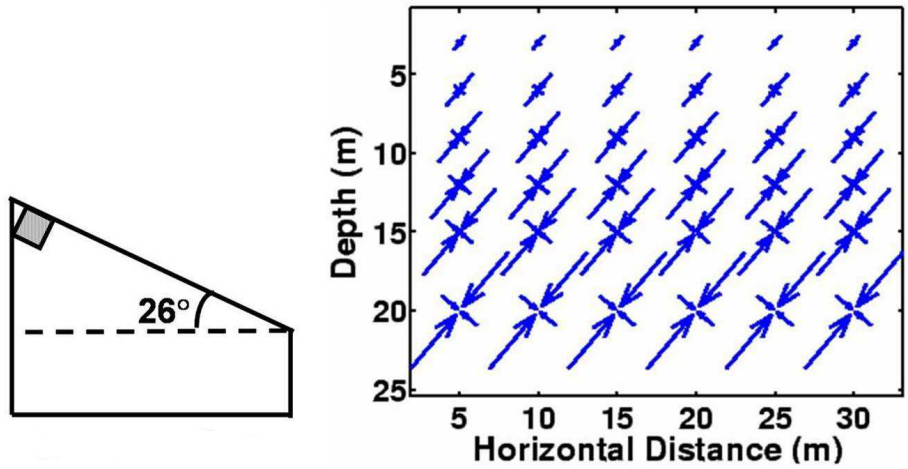

Figure 2.2. In the right panel, principal stress components and directions are plotted for a slope of 26°. The directions of the arrows indicate principal stress directions, while the length of each arrow indicates the magnitude of the principal stress. Inward pointing arrows refer to positive, compressive stress. The shaded area in the left panel indicates the region of the slope shown on the right.

The principal stresses are used to define a circle in normal- and shear-stress coordinates called the Mohr circle of stress. The principal stress components are represented by the intersections of the Mohr circle with the σ-axis, and points on the circle give us values of shear, τ, and normal stress, σ (e.g., Terzaghi *et al.*, 1996). On a plane whose normal makes an angle α with the principal stress direction associated with σ_1:

$$\sigma = \left(\frac{\sigma_1 + \sigma_3}{2}\right) + \left(\frac{\sigma_1 - \sigma_3}{2}\right)\cos(2\alpha)\ , \tag{2.13}$$

$$\tau = \left(\frac{\sigma_1 - \sigma_3}{2}\right)\sin(2\alpha)\ . \tag{2.14}$$

The center of the Mohr circle is located at $(\sigma_1 + \sigma_3)/2$, while the radius of the circle is $(\sigma_1 - \sigma_3)/2$ (Middleton & Wilcock, 1994).

The Mohr circle is the basis for the Mohr-Coulomb failure analysis which tests whether stress exceeds strength in a slope. The shear strength of a failure surface in dry conditions is characterized by the Mohr-Coulomb failure criterion (e.g., Bourne & Willemse, 2001),

$$\tau = c + \sigma \tan(\phi) \ . \tag{2.15}$$

Frictional forces are created from the resistance of particles sliding past each other. When sliding initiates on a surface, the frictional forces are exceeded, and the slope angle will have reached maximum value. This angle is referred to as the internal angle of friction, ϕ (Selby, 1993). As seen in Figure 2.3, the slope of the Mohr-Coulomb envelope is ϕ, which for sands is normally about 30°-34° (Das, 1997; Selby, 1993). Cohesion strengthens a material and typically exists in soils containing clay. It is possible for materials to have zero cohesion, occurring in clean, dry, uncemented sands which do not have the ability to stick together. The values of cohesion for sands used in this analysis are smaller than those for solid rock, and range from 0-20 kPa (Middleton & Wilcock, 1994; Selby, 1993).

Equation 2.15 provides a linear approximation to the Mohr envelope, which is actually a concave-down strength envelope. As shown by Middleton & Wilcock (1994), the straight-line approximation is widely used for the sake of simplicity and provides a good representation for the strength of a material.

Figure 2.3 displays the Mohr circle and Mohr-Coulomb failure envelope. This determines at this location whether stress causes failure. The strength envelope remains the same for the entire slope, but the Mohr circle produced at each location can change due to the difference of dynamic stress in the slope.

Shear failure takes place when the Mohr circle is tangent to the failure envelope. A post-failure state of stress represented by a Mohr circle lying outside of the enve-

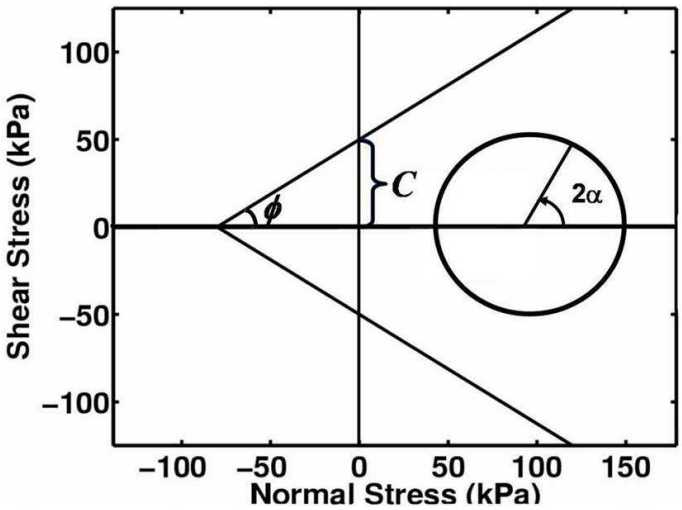

Figure 2.3. Example of the Mohr circle and Mohr-Coulomb failure envelope, which indicate the location of the plotted circle is stable. C is the cohesion of the slope and ϕ is the internal angle of friction. When failure occurs, α refers to the angle between the normal to the failure plane and the principal stress direction corresponding to σ_1.

lope is not physically possible and indicates that shear failure would have occurred previously (Das, 1997). If the circle does not touch the envelope, such as in Figure 2.3, the strength of the slope exceeds the stress, and the slope remains stable. Failure takes place when the critical angle, $\alpha = (90^\circ + \phi)/2$ (Das, 1997).

While the Mohr-Coulomb failure criterion is the leading description of how materials behave under stress, it is only used to describe shear failure (Bourne & Willemse, 2001). This project aims to understand the locations of both shear and tensile failure, therefore, Mohr-Coulomb acknowledges only half of the problem at hand. It is important to explore another failure criterion that accounts for extensional stress and failure. This leads to the Griffith strength envelope.

The hypothesis produced by Griffith in 1921 follows the assumption that solid rock is filled with confined cracks (Brace, 1960). His theory, originally tested in glass,

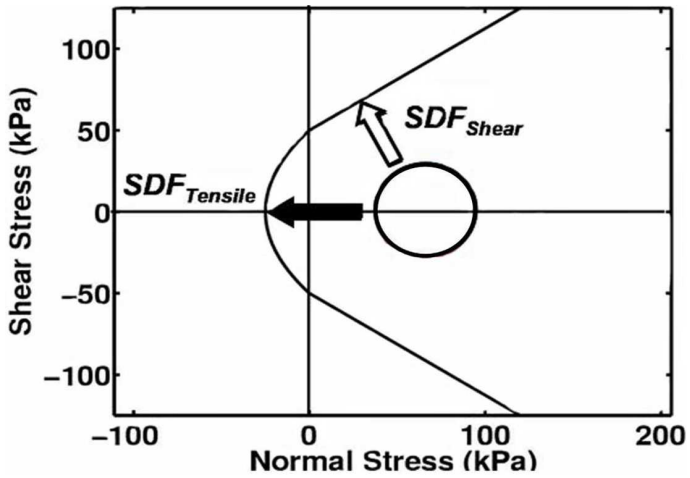

Figure 2.4. Example of the Mohr circle and Mohr-Griffith failure envelope which indicate the location of the plotted circle is stable. The dark arrow shows how far the circle is to failing in a tensile manner indicated by the Griffith portion of the envelope. The white arrow shows the distance the circle is to failing in a shear manner indicated by the Coulomb portion of the envelope.

states that as stress increases near the tips of these thin, elliptical cracks, tensile failure eventually occurs. The tensile strength of a slope follows the parabolic Griffith criterion (Bourne & Willemse, 2001),

$$\tau^2 = 2c\sigma + c^2 \ . \tag{2.16}$$

A cohesionless slope has no tensile strength, therefore the Griffith analysis cannot be utilized for this special case.

A modification of this criterion, called the Modified Griffith Theory, has been introduced by Brace (1960) by combining tensile and shear failure into a single envelope (see Figure 2.4). At small shear stress, the curved part of the envelope is defined by the Griffith equation, describing tensile failure. For larger shear stress, the envelope is defined by the Mohr-Coulomb equation. The region of the failure envelope first

encountered by the Mohr circle determines the type of failure (Bourne & Willemse, 2001). Shear failure takes place when the circle is tangent to the Mohr-Coulomb area and tensile failure within the Griffith section (Bourne & Willemse, 2001). In circumstances where the Mohr circle does not reach the failure envelope, we solve for a stress difference to failure (SDF) by calculating the stress necessary for failure to occur. As shown in Figure 2.4, this stress difference-to-failure quantity gives the proximity of any stress tensor to either shear or tensile failure. Failure takes place when either SDF_{shear} or $SDF_{tensile}$ is equal to zero, whichever occurs first (Bourne & Willemse, 2001). A stable stress state is represented as negative values of SDF, becoming less negative when stress becomes more unstable. The equations to calculate SDF for the modified Griffith envelope are given as (Bourne & Willemse, 2001):

$$SDF_{shear} = \left(\frac{\sigma_1 - \sigma_3}{2}\right) - \left(\frac{\sigma_1 + \sigma_3}{2}\right)\sin(\phi) - c\cos(\phi)\ , \tag{2.17}$$

$$SDF_{tensile} = \left(\frac{\sigma_1 - \sigma_3}{2}\right) - \left(\frac{\sigma_1 + \sigma_3}{2}\right) - \frac{1}{2}c;\, . \tag{2.18}$$

The modified Griffith envelope is currently the accepted method for those working with tensile failure and is used in this project to understand both types of failure. In the next chapter, dynamic stress produced in a homogeneous slope is analyzed using this model.

Chapter 3

HOMOGENEOUS INFINITE SLOPE

In Chapter 2, we define a stress model to describe shear and tensile failure triggered by dynamic stress in a slope. In this chapter, the stress model is used to test how an incoming plane wave disrupts a simple, static slope. The simplest scenario involves an unsaturated slope comprised of homogeneous materials having a constant density of 2,000 kg/m^3 and internal friction angle of 32°. We use various values of cohesion to understand how the strength of the slope influences shear and tensile failure due to an incoming wave.

3.1 Static Slope Analysis

Before modeling the plane wave propagation through a slope, a static slope-stability analysis is carried out for each test criterion to find whether the slope is initially statically stable (Jibson, 1993). This is done by increasing the slope angle to see at which point the slope fails. This way, an incoming wave, generating dynamic stress, will cause failure at slope angles less than those for static instability.

When analyzing a static slope, a discrepancy becomes apparent between this static stress model and other traditional models. Normally, to study the limit-equilibrium of a slope, a factor-of-safety analysis is completed on a static model which produces failure when the FS is 1.0 or below. The factor of safety equation can be defined as:

$$FS = C \; + \; F \; - \; R \, , \tag{3.1}$$

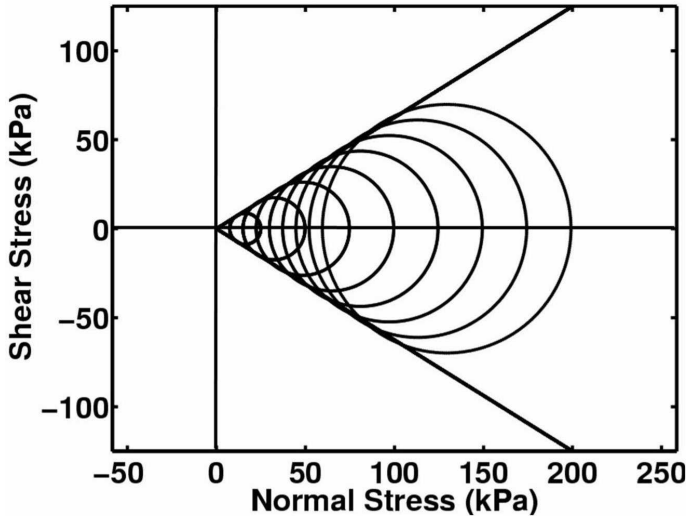

Figure 3.1. Mohr-Coulomb failure envelope and Mohr circles produced by the static stress model at several depths for a 26°, cohesionless slope, where $\phi = 32°$.

where C refers to the cohesive component of strength, F, the frictional component and R as the reduction in frictional strength due to pore pressure (Jibson *et al.*, 2000). For unsaturated conditions, the third term vanishes from equation (3.1), while for a cohesionless case, the first term drops out. Therefore, the FS equation for a dry, cohesionless slope is reduced to the frictional component of the slope,

$$FS = \frac{\tan(\phi)}{\tan(\theta)} \,. \tag{3.2}$$

At the point when ϕ is equal to θ, $FS = 1.0$, indicating slope instability. Given this information, it is not possible for a slope to be inclined at an angle greater than the friction angle (Terzaghi *et al.*, 1996). On the other hand, our model is more conservative, meaning failure takes place at a critical angle, θ, which is less than ϕ. For a slope with $\phi = 32°$, this model predicts static failure at all depths of a slope inclined at 26°, as indicated by the Mohr circles in Figure 3.1. This model also

suggests that given a particular Poisson's ratio, it is possible for horizontal ground to fail. This is explained by elastic theory outlined in Appendix B (V. Griffiths, personal communication, 2005).

We recognize that most slopes are not perfectly cohesionless and that this condition helps to stabilize a slope (Terzaghi *et al.*, 1996). This is why multiple tests are completed to understand how strength plays a role in failure. However, regardless of the amount of cohesion in a slope, there is still a discrepancy with the static model. The assumption of a laterally constrained, infinite slope, used in this model, could be the reason we obtain a critical angle that differs from the internal angle of friction. The horizontal derivatives are assumed to be zero, so material cannot expand in this direction.

It is also possible that as the stress state approaches failure, the assumption of elastic behavior is invalid invalid and becomes an elasto-plastic problem. Plastic behavior of a slope is described in more detail by Savage & Smith (1986). Nevertheless, the assumptions of this stress model are valid, and the equations defining static stress are mathematically correct given these assumptions. Therefore, we work with these equations to understand how dynamic stress affects failure on a static slope.

3.2 Dynamic Analysis

Plane waves, used in this study, are the simplest solution to the wave equation (Aki & Richards, 2002). Plane waves can be divided into two types: P-waves which have particle motion in the direction parallel to propagation and, S-waves, either SH or SV, which have motion normal to the direction of propagation (Selby, 1993). We work with SV-waves, which are referred to as S-waves in this paper. Figure 3.2 shows how a plane P-wave moves through a homogeneous medium producing reflected P-

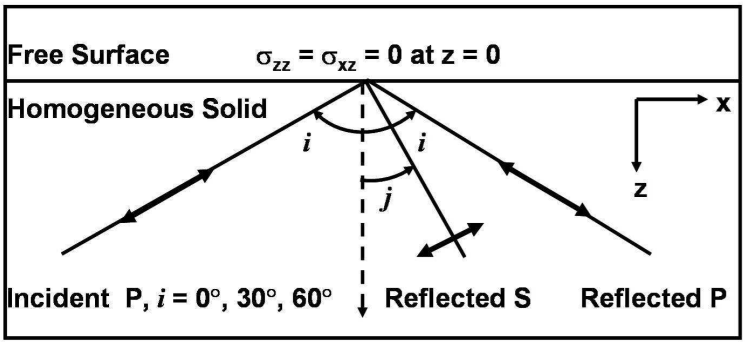

Figure 3.2. P-wave incident on the free surface producing a reflected P- and S-wave. The arrows indicate the direction of wave motion. The incidence angles tested for this project, i, include 0°, 30°, and 60° (modified from Haney, 2004).

and S-waves once hitting the free surface.

The dynamic model illustrates the propagation of a wave by graphing the horizontal or vertical component of displacement of an incoming wave through a homogeneous medium. For example, Figure 3.3 shows the horizontal component of displacement of an S-wave at 30° incidence for an arbitrary slope. The angles in the image are not preserved due to extreme vertical exaggeration needed to show details of the displacement within the slope.

The colors in the image represent the amplitude of displacement with green as zero, red being large amplitude and blue as the negative value of red. The incoming S-wave, shown as the right red streak is generated at depth and propagates in the direction of the free surface with horizontal slowness, p. As the S-wave continues to move across the surface of the slope, it generates reflected waves. The reflected S-wave is shown in this image as the left red streak. The arrows in the image indicate the direction of propagation for each of these wavefronts. The reflected P-wave exists, although is not imaged in this figure because it produces amplitudes that are not in

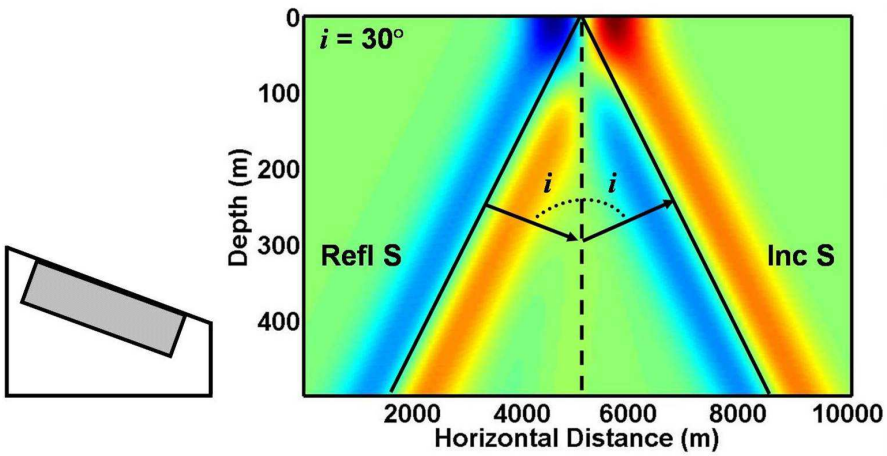

Figure 3.3. In the right panel, the horizontal component of displacement for a 30° incident S-wave normalized to a PGA=0.1 g is shown as the right red streak. As the wave hits the free surface it generates reflected waves, with the reflected S-wave shown here as the red streak on the left. The arrows indicate the direction of propagation of each wave. The angles in this image are not preserved due to vertical exaggeration. The shaded area in the left panel indicates the region of the slope shown on the right.

the range shown here. Because the wave is sweeping across the slope, there may be instances when there is no failure until dynamic stress from the wave is large enough to cause failure at a given instant in time. This is why different locations within the slope will fail at different moments in time.

The peak ground acceleration and frequency of the incoming wave influence the stress generated and, hence, the amount of failure a slope experiences. In this stress model, the acceleration initially produced for an incoming wave must be scaled to a desirable peak ground acceleration (PGA). Normally this acceleration is chosen as a value typical of earthquakes, between 0.1 and 1.0 g (Jibson, 1993). The calibration is done by calculating the sum of the squares of the maximum horizontal a_x, and vertical a_z, acceleration values at the surface of the slope and normalizing to the PGA. The normalization value is then multiplied with the dynamic stress components produced

by the code. For the plane wave in Figure 3.3, the PGA is scaled to 0.1 g.

Harp & Jibson (1995), and Jibson (1993), indicate that an effective PGA will cause failure if it is a larger than the critical acceleration, a_c, of the slope. The critical acceleration a slope can withstand is found by equation (1.1), used in Newmark's analysis. To find a_c, the FS and slope geometry of the slope need to be known.

Failure depends on the PGA of the incoming wave, and for each slope, there exists a PGA that causes the origination of failure at one location for a given instant in time. As the PGA increases, post-failure occurs, and the extent of the post-failure area increases with increasing slope angle. For these post-failure locations, we cannot trust the stress and displacement produced by the numerical code. More importantly, when altering the PGA, the mechanism of failure does not change in a slope. Therefore, we work with a small PGA to avoid regions of post-failure in this analysis.

The U. S. Geological Survey provides a useful mapping tool for shaking intensity levels produced by each major earthquake. These ShakeMaps are made available to the public by combining information such as the recorded PGA and peak velocity values for locations surrounding the epicenter of the earthquake and give the spatial distribution of perceived shaking and damage produced by a particular earthquake (Wald *et al.*, 1999). This product tells us whether the PGA of 0.1 g, used in Figure 3.3, is a realistic value for slope failure.

Because the Northridge, California earthquake in 1994 is known as an extensive landslide triggering event, the ShakeMap for this event is used to find the PGA values recorded by this earthquake. This helps us evaluate if 0.1 g produces landslides in a region typical of earthquake hazards. The PGA experienced in the region of the Northridge earthquake is displayed in Figure 3.4. Contours indicate the percent of

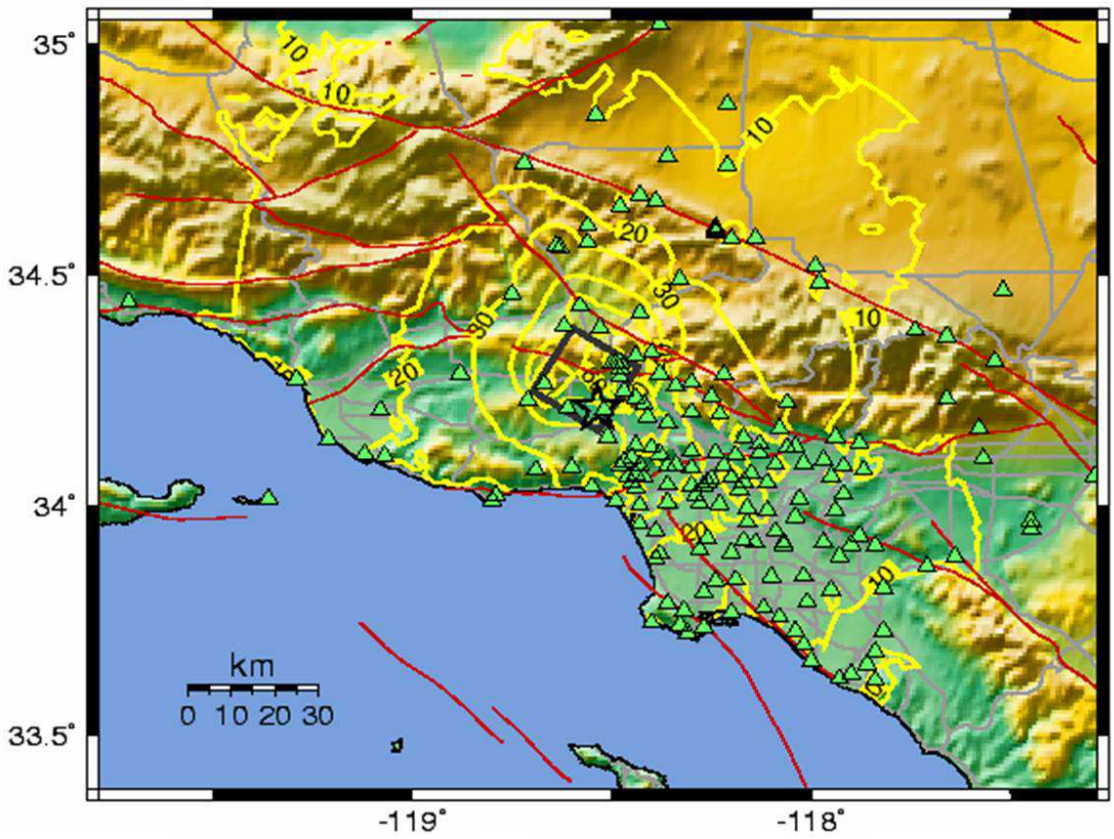

Figure 3.4. ShakeMap for the 1994 Northridge, California earthquake displaying peak ground acceleration values for locations surrounding the epicenter, indicated by the star. Contours indicate the percent of gravitational acceleration experienced at the surface (Wald *et al.*, 1999).

gravitational acceleration. This shows accelerations of 0.1 g at distances about 50-60 km and greater from the epicenter. Jibson *et al.* (2000) shows the spatial distribution of landslides triggered in the Northridge region, which includes a portion of the area that experienced 0.1 g, while the largest concentration of slides were triggered by 0.6 g. Therefore, we feel comfortable that the conservative value of 0.1 g is valid for testing failure and is used in all future examples.

The frequency of the incoming wave is also defined for the model. Proper design of earthquake-resistant structures require estimation of ground shaking in the 0.2-10 Hz frequency band (Frankel, 1999). We work with a moderate peak frequency of 1.0 Hz.

P- and S-waves may produce different failure mechanisms within a slope, therefore both are analyzed. When each is normalized to the same PGA, the S-wave produces larger dynamic stress at the surface of the slope than does the P-wave. To explain this, we examine the displacement due to P- and S-waves from an earthquake source, which depend on the inverse cube of the P- and S-wave velocities, α and β,

$$u^p \propto \frac{1}{4\pi\rho\alpha^3} \propto \frac{1}{\alpha^3} \ , \tag{3.3}$$

$$u^s \propto \frac{1}{4\pi\rho\beta^3} \propto \frac{1}{\beta^3} \ , \tag{3.4}$$

where ρ is density (Aki & Richards, 2002). Stress is related to displacement through Hooke's Law:

$$\sigma \propto (\textit{Lamé constant})\nabla u \ . \tag{3.5}$$

The gradient of displacement is multiplied with the elastic constant for either a P- or S-wave,

$$\sigma^p \propto (\lambda + 2\mu)\frac{\omega}{\alpha}u^p \ , \tag{3.6}$$

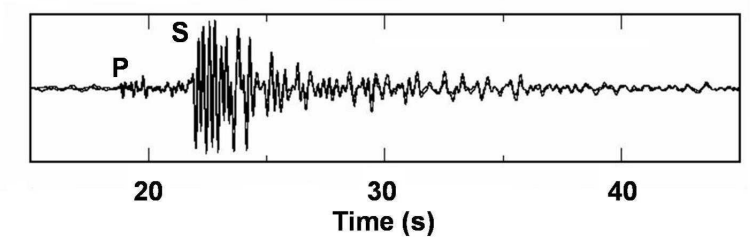

Figure 3.5. Seismogram for an event on the Hayward fault in California recorded by the Northern California Seismic Network. This data provides evidence that the S-wave arrival, marked as S, has larger amplitude than the P-wave arrival (from Snieder & Vrijlandt, 2005).

$$\sigma^s \propto \mu \frac{\omega}{\beta} u^s \ , \tag{3.7}$$

where ω is angular frequency. Because $(\lambda + 2\mu) = \alpha^2 \rho$, and $\mu = \beta^2 \rho$, stress is related to P- and S-wave velocities by substituting displacement relations (3.3-3.4):

$$\sigma^p \propto \alpha^2 \rho \frac{1}{\alpha} u^p \propto \alpha \frac{1}{\alpha^3} \propto \frac{1}{\alpha^2} \ , \tag{3.8}$$

$$\sigma^s \propto \beta^2 \rho \frac{1}{\beta} u^s \propto \beta \frac{1}{\beta^3} \propto \frac{1}{\beta^2} \ . \tag{3.9}$$

According to these equations, the stress produced by an S-wave is larger because the velocity for the S-wave is smaller than for the P-wave. To confirm equations (3.8) and (3.9), Figure 3.5 displays a seismogram recorded by the Northern California Seismic Network for an event on the Hayward fault in California (Snieder & Vrijlandt, 2005). These data show that the P-wave arrival, marked with P, has smaller amplitude than the S-wave arrival.

Figure 3.6 provides a comparison of stress produced by 30° incident P- and S-waves with the numerical code. This shows that after both waves are calibrated to

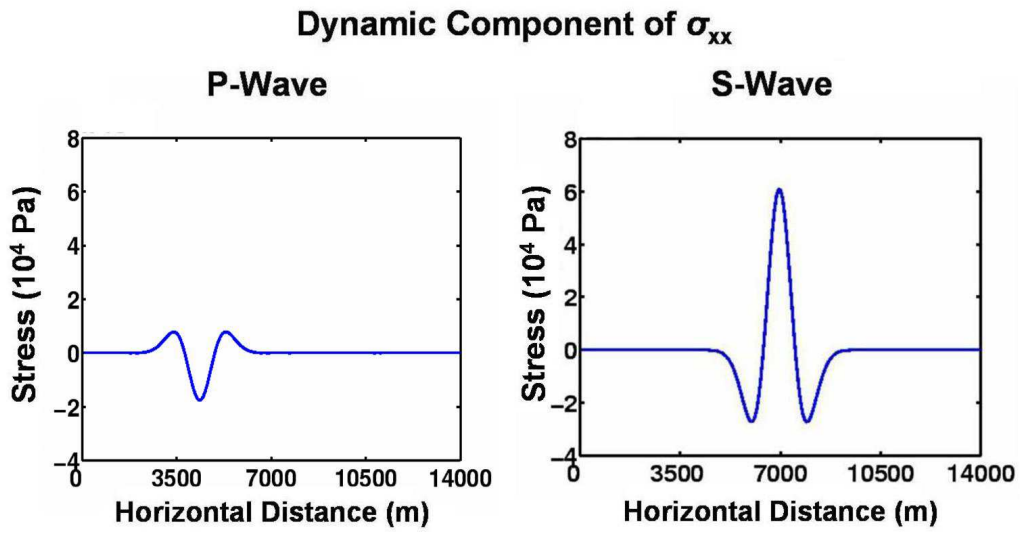

Figure 3.6. $\sigma_{xx}^{dynamic}$ component of stress for both 30° incident P- and S-waves at the surface of a slope. After both waves are calibrated to a PGA of 0.1 g, the S-wave produces larger stress at the surface than the P-wave.

a PGA of 0.1 g, the $\sigma_{xx}^{dynamic}$ component of stress at the surface is greater for the S-wave than for the P-wave. Reflected waves generated at the free surface of the slope also influence dynamic stress produced at this location. Overall, the S-wave produces larger stress at the surface, making it more likely to create failure than the P-wave does. Therefore, we examine how failure is influenced by the dynamic stress of an S-wave propagating through a slope.

After testing a variety of incidence and slope angles, the analysis of failure due to an S-wave demonstrates that both shear and tensile failure may occur in a slope. Shear failure takes place at depth within a homogeneous slope while tensile failure also occurs at shallow locations near the surface. This type of behavior takes place for the tested incidence angles of 30° and 60° in a cohesive slope. For a given ground

acceleration, a 60° incident wave produces regions of post-failure throughout a slope, while a 30° incident wave produces initial shear and tensile failure. Therefore, we analyze the 30° incident wave in this project.

For a normally incident wave, all static and dynamic stress components are zero at the surface. Because this is the location where tensile failure is produced from the $\sigma_{xx}^{dynamic}$ component of stress due to non-zero incident waves, it is not possible for this mechanism of failure to be generated due to the lack of stress. A wave with normal incidence only produces shear failure in a slope.

The examples that follow provide evidence of shear and tensile failure following propagation of a plane wave through a slope for a given instant in time. These examples demonstrate the properties failure is dependent on, and the locations of failure in a slope.

3.3 Tensile Failure for Incoming S-Wave

As stated previously, tensile failure occurs at the surface of slopes containing cohesion when a non-normally incident wave disrupts a statically stable slope. Figure 3.7 provides an example of tensile failure due to the 30° incident S-wave normalized to a PGA of 0.1 g. Before dynamic stress disrupts the slope, failure of the static slope with $c = 10$ kPa and $\phi = 32°$, takes place at 37°. When a slope is cohesive, such as in this example, static failure can occur at a slope angle larger than the internal angle of friction.

An indication of shear failure due to this dynamic stress is found at a depth of 10 m for a 20° slope. At this angle, the static stress is large enough at depth that, when combined with dynamic stress, causes failure. There is no indication of tensile failure here because at shallower depths, the strength of the slope exceeds stress. As

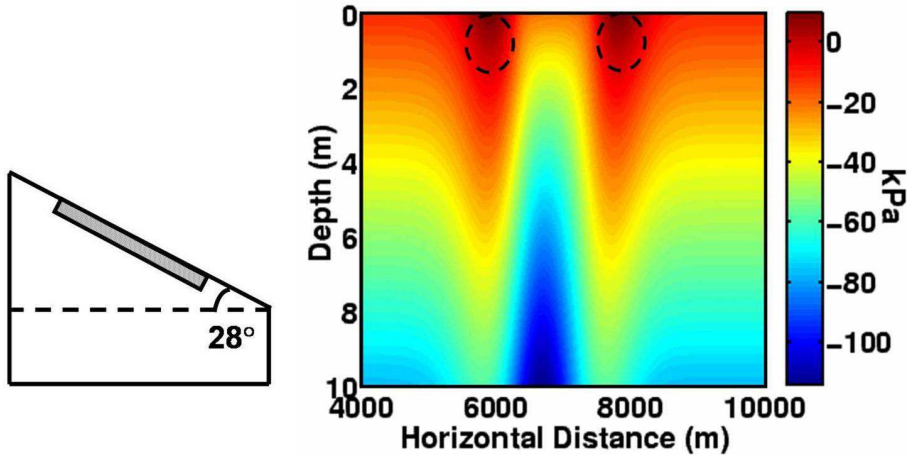

Figure 3.7. In the right panel, the stress difference to tensile failure is displayed for a slope of 28° and $c = 10$ kPa due to a 30° incident S-wave normalized to a PGA=0.1 g. The shaded area in the left panel indicates the region of the slope shown on the right. Failure occurs at the near surface, indicated by the circled regions. Negative values indicate the amount of stress necessary for tensile failure to occur.

the slope angle increases, stress in the upper meters of the slope exceed strength and tensile failure takes place at 28°. Figure 3.7 shows the stress difference to tensile failure for this slope.

For a given instant in time, dynamic stress is great enough to produce tensile failure. The circled areas in dark red near the surface of the slope show the locations which have failed using the modified Griffith criterion. The colorbar also indicates that there are a few locations in dark red which surpass initial failure, or, those locations that have a positive $SDF_{tensile}$. All other locations within the

Evidence for failure in this slope can be found by analyzing the principal stress components and directions calculated after dynamic stress is added at each location to the static stress. Figure 3.8 shows the principal stresses for the 28° slope. Outward pointing arrows near the surface indicate tensile stress, that which causes tensile

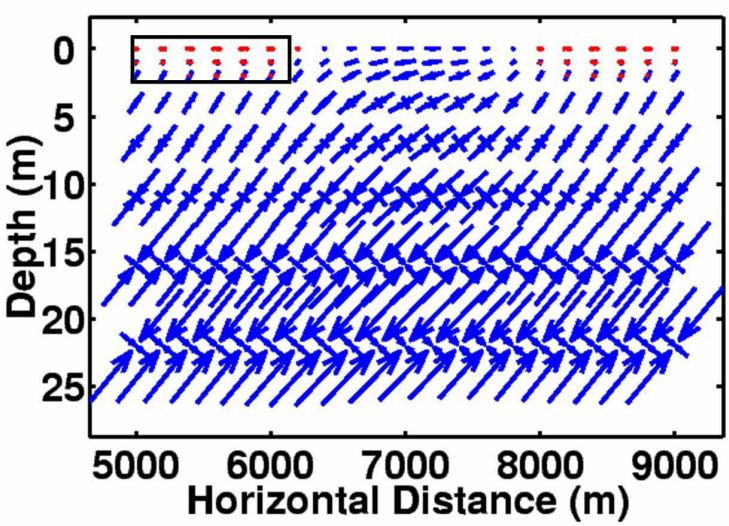

Figure 3.8. Principal stress components and directions computed for a segment of the 28° slope shown in Figure 3.7 due to a 30° incident S-wave normalized to a PGA=0.1 g. Inward pointing arrows represent compressional stress, while outward pointing arrows indicate extensional stress, noticeable at the near surface where tensile failure is found. The box is enlarged in Figure 3.9.

failure seen in Figure 3.7. The behavior of tensile stress is of importance and so the box in this image is enlarged for clarity. slope have not failed, producing a negative $SDF_{tensile}$.

Figure 3.9 shows principal stresses near the surface for the slope shown in Figure 3.7, focusing on the specific area that has tensile failure. At the surface, only tensile stress exists, indicating a scenario that leads to tensile failure.

At 1 m depth, both compressional and extensional stresses exist. The maximum principal stress is compressive, slightly larger in magnitude than the tensile minimum principal stress. Figure 3.10 shows the Mohr circle at this depth and a horizontal distance of 5,500 m. Here, the stress difference to tensile failure is zero, with a large part of the circle touching the Griffith region of the envelope. In this case, the actual

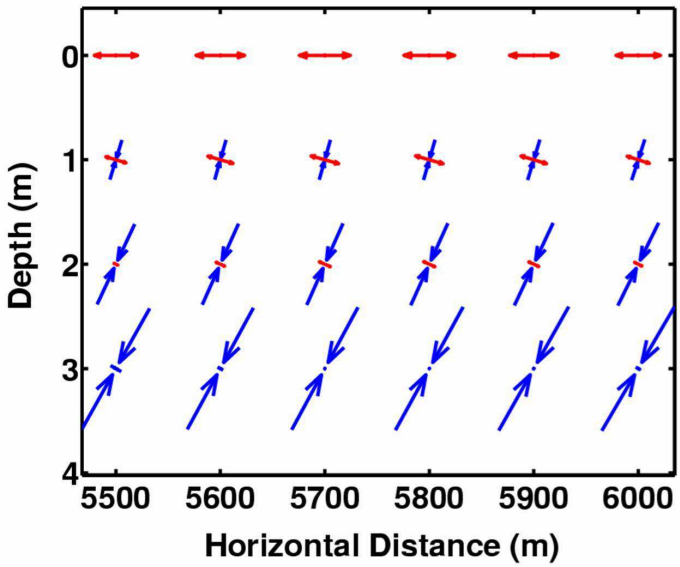

Figure 3.9. Principal stresses for a segment of the 28° slope shown in Figure 3.7 due to a 30° incident S-wave normalized to a PGA=0.1 g. Tensile stress exists to a depth of 2 m. Below a depth of 3 m, compressive stress is dominant.

failure plane is poorly defined since the circle touches the envelope in more than one location.

The stresses at 2 m depth show a slight indication of extensional stress, although the dominant stress is compressive. At this depth, tensile failure does not occur. At 3 m, there is no tensile stress since both principal stress components are larger than zero, further reducing the possibility for tensile failure to occur at this depth.

Now that it is evident that tensile failure may occur within a slope, we focus on what is causing failure. There are six stress components acting on the slope at any given location: σ_{xx}^{static}, σ_{zz}^{static}, σ_{xz}^{static}, $\sigma_{xx}^{dynamic}$, $\sigma_{zz}^{dynamic}$, $\sigma_{xz}^{dynamic}$. Figure 3.11 displays these stress components as a function of depth at a horizontal distance of 5,500 m. This shows that all components of stress, σ^{static} and $\sigma^{dynamic}$, go to zero at the surface except one, $\sigma_{xx}^{dynamic}$, shown in red. The three components of static

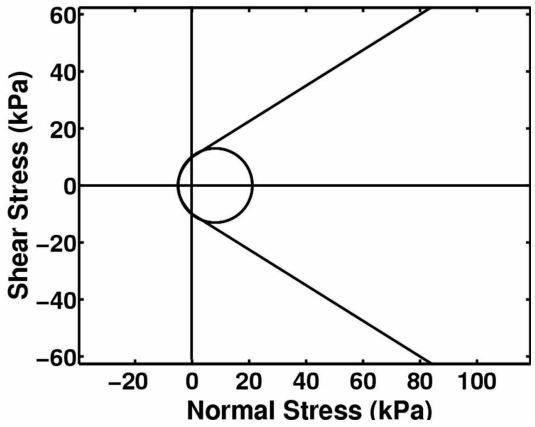

Figure 3.10. Mohr circle produced at a depth of 1 m and horizontal distance of 5,500 m for the 28° slope in Figure 3.7. This circle is created in the same location where tensile failure occurs in the $SDF_{tensile}$ image.

stress depend on depth, as given in equations (2.2-2.4), and at the surface are equal to zero. Similarly, the two dynamic components $\sigma_{xz}^{dynamic}$ and $\sigma_{zz}^{dynamic}$ vanish at the free surface due to boundary conditions, leaving $\sigma_{xx}^{dynamic}$ as the only non-zero stress component. For cases involving normally incident waves, all stress components go to zero at the surface and tensile failure cannot occur.

Therefore, at the surface of this slope, tensile failure must be directly related to $\sigma_{xx}^{dynamic}$. At a certain depth, where compressive static stress dominates dynamic tensile stress, tensile failure does not occur. We further analyze the depth of tensile failure by studying derived dynamic stress equations.

3.4 Dynamic Stress Near the Surface

We derive dynamic stress equations independent of the dynamic stress produced by the numerical code. These stress equations originate from Newton's Law and Hooke's Law with the purpose of knowing the dynamic 2D stress in the near surface

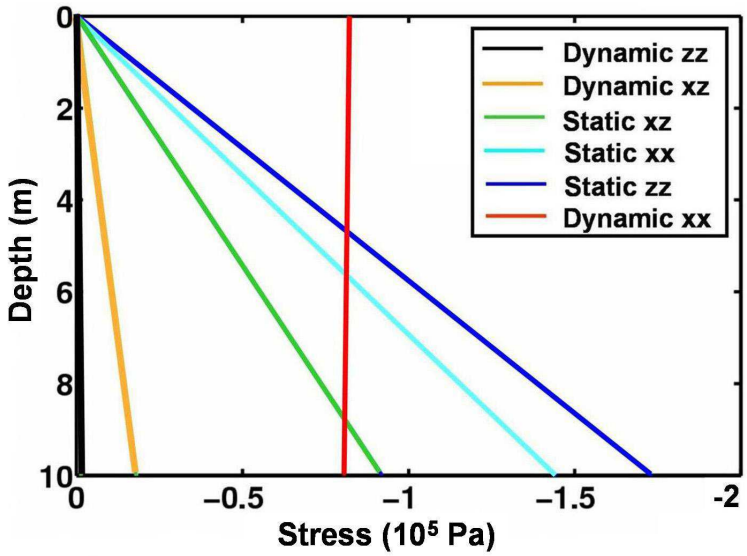

Figure 3.11. Stress components as a function of depth at a horizontal distance of 5,500 m for the 28° slope shown in Figure 3.7. All stress components, σ^{static} and $\sigma^{dynamic}$, go to zero at the surface except for $\sigma_{xx}^{dynamic}$, shown in red. At the surface, this is the stress component dominant in creating tensile failure in the x-direction. As static stress becomes larger with depth, tensile failure does not occur.

given measurements of displacement at the surface of the slope. The significance of these equations is to determine the dynamic stress at depth when the PGA and direction of an incoming wave are known. The derivation of the equations for σ_{xx}^{dyneq}, σ_{zz}^{dyneq}, σ_{xz}^{dyneq} can be found in Appendix C:

$$\sigma_{xx}^{dyneq}(z) = \frac{4\mu(\lambda+\mu)}{\lambda+2\mu}\left(\frac{p}{2\pi f}\right)a_x \ , \tag{3.10}$$

$$\sigma_{zz}^{dyneq}(z) = -\rho a_z z \ , \tag{3.11}$$

$$\sigma_{xz}^{dyneq}(z) = -\left\{\rho a_x + \left(\frac{4\mu(\lambda+\mu)}{\lambda+2\mu}\right)\left(\frac{p}{2\pi f}\frac{\partial a_x}{\partial x}\right)\right\} z \ , \tag{3.12}$$

where p is the horizontal slowness of the incoming wave, f the peak frequency, a_x the acceleration in the horizontal direction, and a_z the acceleration in the vertical direction. At the surface, these equations produce stress components $\sigma_{zz}^{dyneq}(z=0) = \sigma_{xz}^{dyneq}(z=0) = 0$, while $\sigma_{xx}^{dyneq}(z=0)$ can be nonzero.

We verify that these equations are a good approximation of the dynamic stress produced by the model by comparing how each stress component behaves with depth, like that shown in Figure 3.11. Using this example, Figure 3.12 displays σ^{static}, $\sigma^{dynamic}$ and σ^{dyneq} for each component of stress. The blue lines represent σ^{static} with depth, black as $\sigma^{dynamic}$, modeled from the wave equation code, and red as σ^{dyneq}, derived from equations (3.10-3.12). σ_{xx}^{dyneq} is constant with depth, and is only slightly different than $\sigma_{xx}^{dynamic}$, which varies slowly with depth. σ_{xx}^{dyneq} is also non-zero at the surface, which is an important comparison to $\sigma_{xx}^{dynamic}$, since this component of stress is responsible for producing tensile failure.

In addition, these equations provide useful information for understanding the limited depth of tensile failure indicated in Figure 3.7. Figure 3.13 displays the same graph in Figure 3.11, although in this case, dynamic stress components are represented

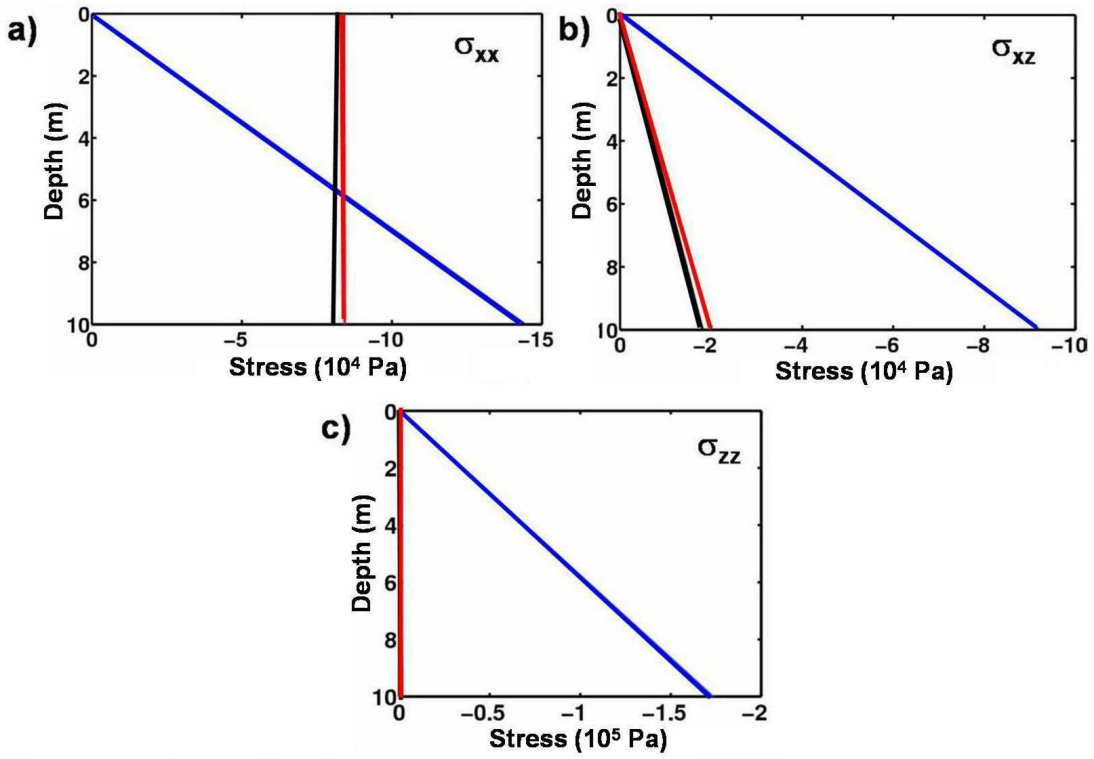

Figure 3.12. Stress components as a function of depth for the example in Figure 3.11. Blue lines represent σ^{static} stress, black as $\sigma^{dynamic}$ and red, σ^{dyneq}, each with depth. a) σ_{xx} component of stress. Similar to $\sigma_{xx}^{dynamic}$, σ_{xx}^{dyneq} is the only non-zero stress at the surface. b) σ_{xz} component of stress. c) σ_{zz} component of stress, where σ_{zz}^{dyneq} and $\sigma_{zz}^{dynamic}$ are identical.

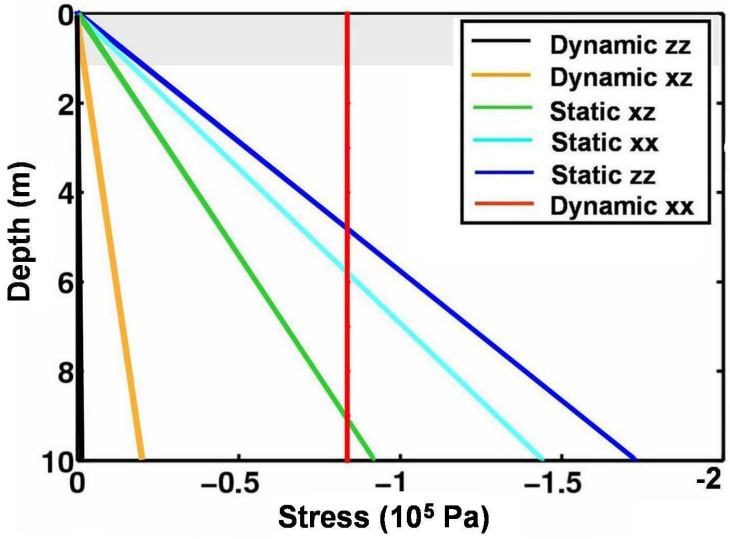

Figure 3.13. Stress components as a function of depth for the same example shown in Figure 3.11. In this figure the dynamic stress equations are used in place of the dynamic stress produced by the model. These stress components help to understand the limited depth of tensile failure for the 28° slope, indicated by the shaded region.

by the dynamic stress equations (3.10-3.12) with depth. The shaded region indicates the depth of initial tensile failure provided from Figure 3.7.

To further understand what the depth of tensile failure depends on, we make the assumption that failure takes place when $\left|\sigma_{xx}^{dyneq}\right|$ is greater than σ_{zz}^{static}. σ_{zz}^{static} is chosen since this is the next largest stress near the surface, and it increases faster than any other stress component with depth.

$$\left|\sigma_{xx}^{dyneq}\right| > \sigma_{zz}^{static} \,, \tag{3.13}$$

substituting the static stress equation for σ_{zz}^{static} (2.3) gives:

$$\left|\sigma_{xx}^{dyneq}\right| > \rho g z \cos(\theta) \,, \tag{3.14}$$

and solving for the depth of failure,

$$z < \frac{\sigma_{xx}^{dyneq}}{\rho g \cos(\theta)} \ . \tag{3.15}$$

At the point of failure, stress has to equal or overcome the strength of the slope. Because σ_{xx}^{dyneq} is constant with depth, and the only source of stress causing tensile failure, it's value is approximately equal to tensile strength, represented by $c/2$,

$$\sigma_{xx}^{dyneq} \approx \frac{c}{2} \ , \tag{3.16}$$

and substituting this into equation (3.15) gives:

$$z < \frac{c}{2\rho g \cos(\theta)} \ . \tag{3.17}$$

Therefore, the depth of tensile failure depends on the tensile strength of the slope, and varies with density and slope angle. For this example, c =10 kPa, $\rho = 2,000$ kg/m^3 and $\theta = 28°$ and from (3.17) the region of tensile failure is estimated to be $z < 0.3$ m. A slope with larger cohesion has a greater depth of tensile failure. For example, if the cohesion within the slope is increased to 50 kPa, the depth of tensile failure is approximately 1.4 m.

This analysis gives a crude estimate of the maximum depth of tensile failure without analyzing $SDF_{tensile}$. It is in this region that the first instance of tensile failure is expected to occur. As σ_{xx}^{dyneq} remains constant, and static stress increases with depth, there is a point where tensile failure no longer occurs due to the growth of compressive, static stress. This is a depth where static stress is large enough so that σ_{xx}^{dyneq} does not make a notable impact for tensile stress in the x-direction. This

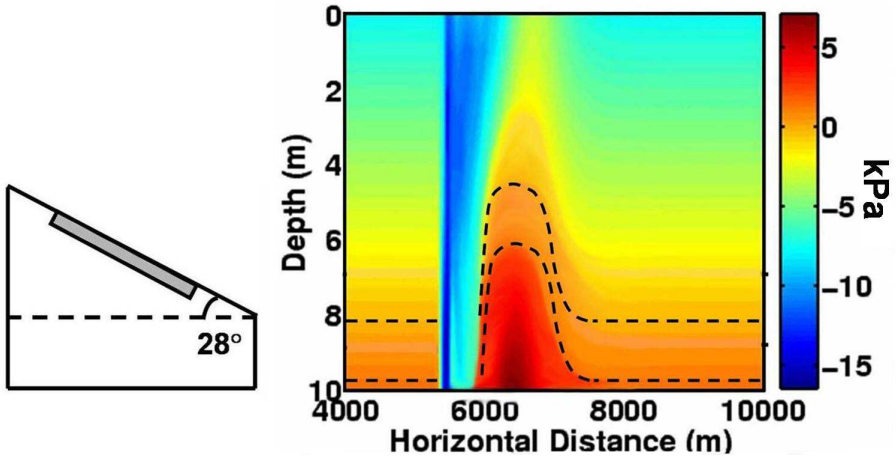

Figure 3.14. In the right panel, the stress difference to shear failure is displayed for a slope of 28° and $c = 10$ kPa due to a 30° incident S-wave normalized to a PGA=0.1 g. The shaded area in the left panel indicates the region of the slope shown on the right. Initiation of shear failure is located between the dotted lines. Negative values of stress represent locations that have not failed and positive values of stress represent those in post-failure, a situation that is not taken into consideration for this project.

analysis not only helps to understand the limited depth of tensile failure, but can also be used for evaluating the depth associated with shear failure in this slope.

3.5 Shear Failure for Incoming S-Wave

Traditionally, methods created to monitor dynamically triggered landslides focus on only one mechanism of failure, shear failure. Terzaghi *et al.* (1996) mentions that shear failure is the only failure mechanism that requires consideration. The goal of this research is to show that both shear and tensile failure occur and to distinguish the locations of each type of failure. Next, we explore the depth of shear failure.

Figure 3.14 displays the stress difference to shear failure for the same slope and incoming wave as Figure 3.7. In addition to tensile failure occurring at the surface of the 28° slope, shear failure is dominant at deeper locations.

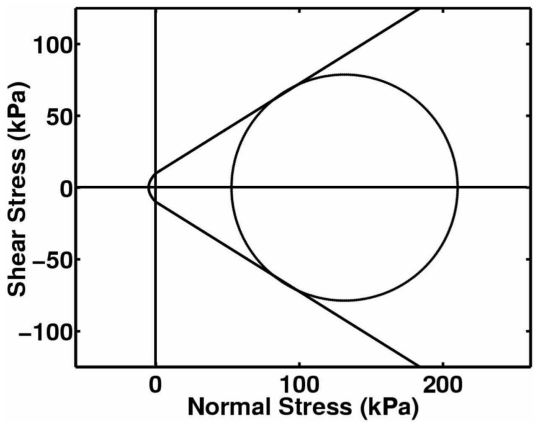

Figure 3.15. Mohr circle for a depth of 9 m and a horizontal distance of 8,000 m for the 28° slope in Figure 3.14. This circle is created in the same location where shear failure occurs in the SDF_{shear} image.

Those areas that are at the point of shear failure, are located approximately within the dotted lines, showing a limited depth of initial failure. The Mohr circle representing failure at a depth of 9 m and horizontal distance of 8,000 m, is shown in Figure 3.15. This image shows that the initiation of shear failure takes place in a region of compressive stress.

These figures demonstrate that shear failure takes place at a greater depth than tensile failure does. For a cohesionless slope, or a slope subject to a normally incident plane wave, shear failure is the only mechanism of failure to occur.

To understand the depth of shear failure, we consider the stress as a function of depth. Figure 3.16 shows the same graph in Figure 3.13, but this time the shaded area indicates the region of shear failure. This graph substitutes σ^{dyneq} for dynamic stress as before, and with this information, the depth of shear failure can be analyzed.

When shear failure takes place, all static stress components are larger than dynamic stress. We characterize initial failure at the depth when the smallest static

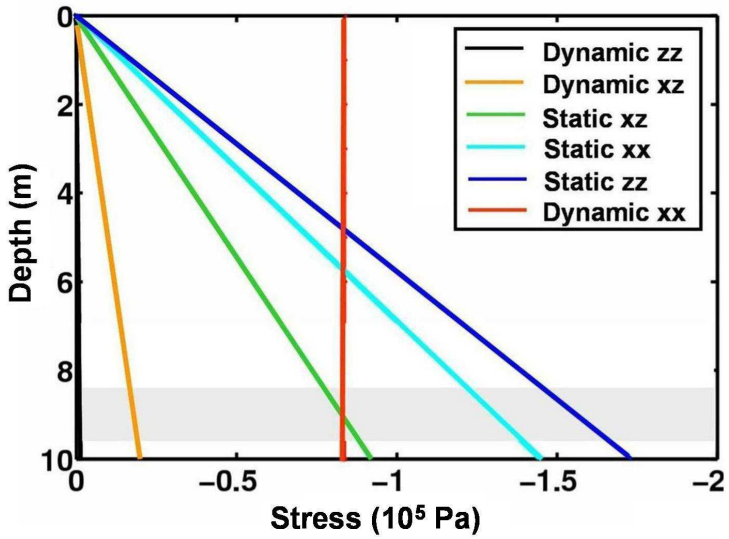

Figure 3.16. The same graph of stress produced for Figure 3.13. The shaded area now indicates the approximate region of shear failure. The dynamic stress components are represented by the dynamic stress equations with depth.

stress component σ_{xz}^{static}, is approximately equal to the largest dynamic stress, σ_{xx}^{dyneq}:

$$\sigma_{xx}^{dyneq} \approx \sigma_{xz}^{static} \ . \tag{3.18}$$

Substituting the static stress equation for σ_{xz}^{static} (2.4) gives:

$$\sigma_{xx}^{dyneq} \approx \rho g z \sin(\theta) \ , \tag{3.19}$$

and solving for depth,

$$z \approx \frac{\sigma_{xx}^{dyneq}}{\rho g \sin(\theta)} \ . \tag{3.20}$$

The depth of failure can be found by substituting dynamic stress equation (3.10) for

σ_{xx}^{dyneq},

$$z \approx \frac{\frac{4\mu(\lambda+\mu)}{\lambda+2\mu}\left(\frac{p}{2\pi f}\right)a_x}{\rho g \sin(\theta)} \; . \tag{3.21}$$

The input parameters for this example are $\lambda = 5.0 \times 10^8$ Pa, $\mu = 5.0 \times 10^9$ Pa, $p = 0.000289$ s/m, $f = 1.0$ Hz, and, $a_x = 0.981$ m/s^2. Because a_x is equal to the normalized PGA value for this example, a_z is negligible, which shows that the dominant contribution to acceleration is in the x-direction, the direction of particle motion for the S-wave. Given this information, $z \approx 9.0$ m for initial shear failure. Equation (3.21) demonstrates that the depth of shear failure relies on many factors, mainly the PGA, as well as the horizontal slowness which depends on incidence angle and velocity of the incoming wave.

This analysis relates the depths of shear and tensile failure in the slope to the dependence of dynamic stress with depth. Statically, the entire slope at 28° is stable, but when a plane wave is incident on the slope, σ_{xx}^{dyneq} becomes the largest dynamic stress responsible for creating both tensile and shear failure. In the near-surface, this component of extensional stress creates tensile failure in the x-direction. Deeper into the slope, σ_{xx}^{dyneq} is still the only notable dynamic stress, but it is less in magnitude than static stress. When each component of stress is positive, tensile failure can no longer take place. When compressive stress is large enough and combined with σ_{xx}^{dyneq}, shear failure occurs. In this example, this takes place near 9 m depth. At a particular depth when $\sigma_{xz}^{static} > \sigma_{xx}^{dyneq}$, failure no longer occurs. Dynamic stress does not grow as quickly as static stress with depth, as seen in Figure 3.16. Therefore, when dynamic stress is small compared to the large static stress of the slope, it has little influence on the total stress field. It is at this depth when dynamic stress does not trigger failure.

With knowledge of the PGA value, the set of static and dynamic stress equations can be used to test for depths of both shear and tensile failure independently. Now

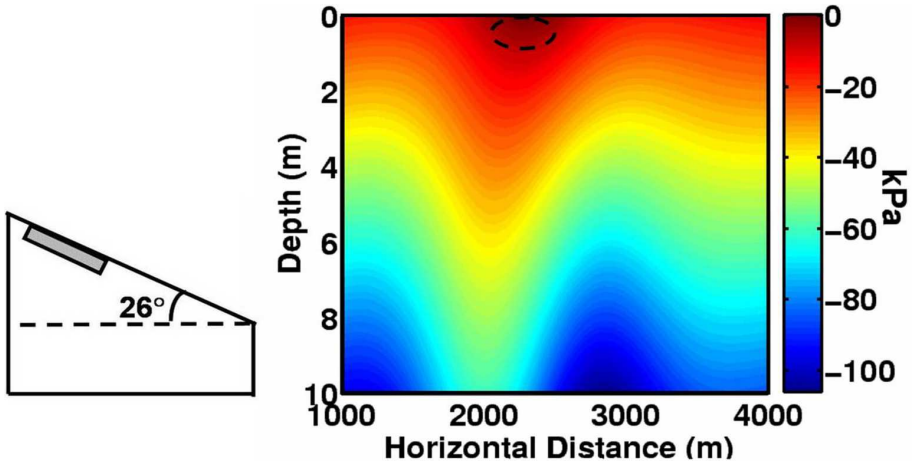

Figure 3.17. In the right panel, the stress difference to tensile failure is displayed for a slope of 26° and $c = 10$ kPa due to a 30° incident P-wave normalized to a PGA=0.1 g. The shaded area in the left panel indicates the region of the slope shown on the right. Failure occurs at the near surface, indicated by the circled region. Negative values indicate the amount of stress necessary for tensile failure to occur.

that it is clear that both shear and tensile failure occur in a slope subject to an S-wave, the next step is to study dynamic failure for an incoming P-wave.

3.6 Incoming P-Wave

Even though an S-wave generates larger stress at the surface, a P-wave normalized to the same PGA produces the same two failure mechanisms as does the S-wave. Thus, regardless of the type of plane wave, P or S, failure occurs in the same manner. The following examples support these findings for both shear and tensile failure in a slope due to a 30° incident P-wave normalized to 0.1 g.

Figure 3.17 demonstrates the stress difference to tensile failure due to this P-wave for a slope of 26°. Again, the cohesion is set to 10 kPa and $\phi = 32°$. Although failure takes place at a different slope angle than for the S-wave, static failure for this slope

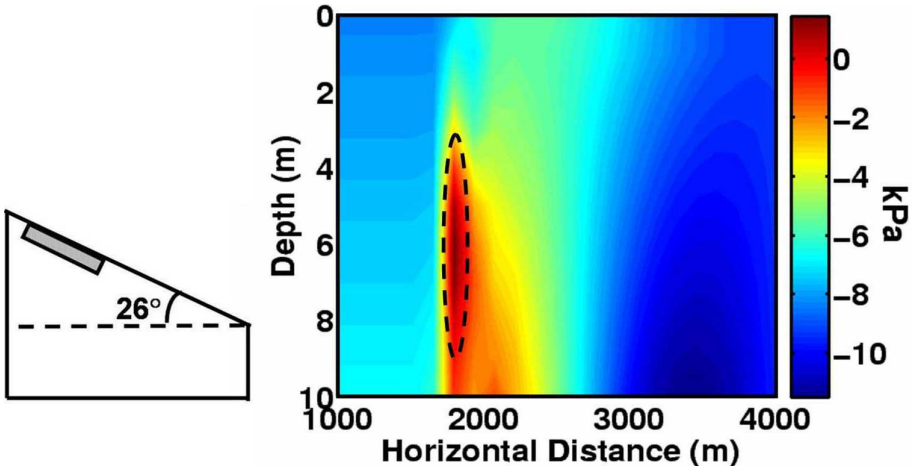

Figure 3.18. In the right panel, the stress difference to shear failure is displayed for a slope of 26° and $c = 10$ kPa due to a 30° incident P-wave normalized to a PGA=0.1 g. Initiation of shear failure is located within the dotted lines. Negative values of stress represent locations have not failed and positive values of stress represent those in post-failure.

remains the same at 37°. The circled region in dark red shows the location for initial tensile failure. As with the S-wave, tensile failure only occurs in the near surface.

Shear failure, as seen in Figure 3.18, takes place at depth. There is a limited depth interval for shear failure at this instant in time with a region above and below the failure zone that is not failing. The approximate location failing in shear is circled.

Figures 3.19-3.20 show the principal stress components and directions computed for this slope. These figures closely resemble the case outlined for failure due to the incident S-wave. Tensile stress is located at the near surface up to 1 m depth, which produces tensile failure in the slope. At shallow depth, compressional stress dominates, and the slope becomes prone to failing in shear.

To investigate these depths of failure more closely, Figure 3.21 shows each stress component with depth. This graph is created for the 26° slope at a horizontal distance

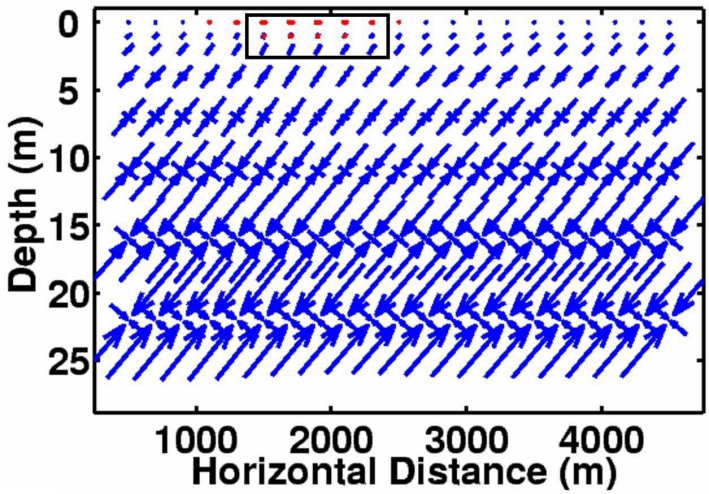

Figure 3.19. Principal stress components and directions computed for the 26° slope shown in Figure 3.17 due to a 30° incident P-wave normalized to a PGA=0.1 g. Inward arrows represent compressional stress, while outward pointing arrows indicate extensional stress, noticeable at the near surface where tensile failure is found. The box is enlarged in Figure 3.20.

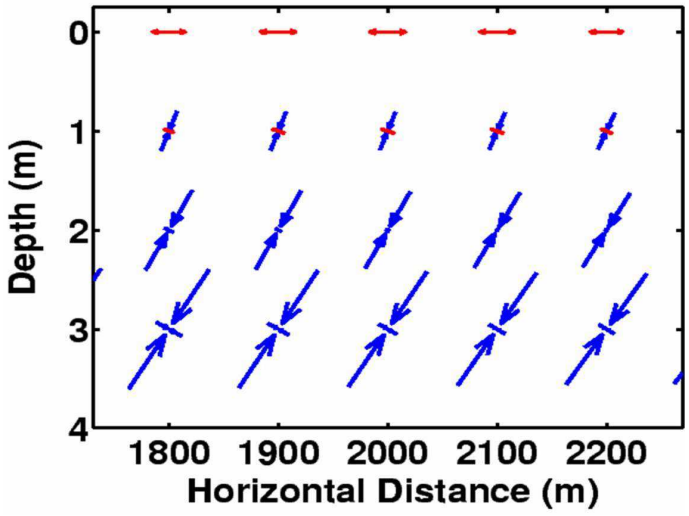

Figure 3.20. Principal stresses for a segment of the 26° slope shown in Figure 3.17. Similar to the S-wave example, this shows that tensile stress exists to a depth of 1 m. At 2 m depth, compressional stress becomes more dominant and the slope is prone to shear failure.

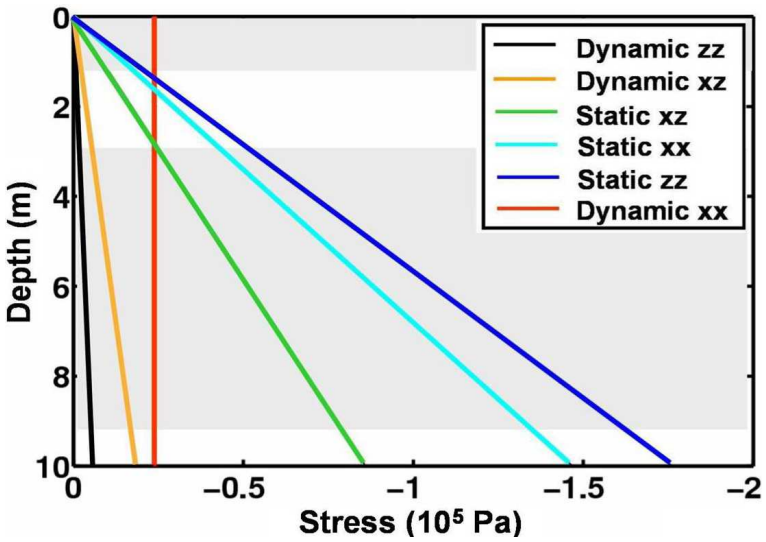

Figure 3.21. Stress components as a function of depth for the example outlined in Figures 3.17-3.18, at a horizontal distance of 2,000 m. Tensile failure for this 26° slope is outlined by the upper shaded region, while shear failure takes place in lower shaded region. The dynamic stress components are represented by the dynamic stress equations with depth.

of 2,000 m, where the dynamic stress equations are used in place of the dynamic stress produced by the model. The region of tensile failure is shaded at the near surface, and the region for shear failure is shaded at depth. The same principles hold for the depth of failure as for the S-wave case. The depth of tensile failure is related to $\left|\sigma_{xx}^{dyneq}\right| > \sigma_{zz}^{static}$, following equation (3.17). Only the slope angle changes in this example, from 28° to 26°, to provide a depth $z < 0.3$ m.

The initiation of shear failure occurs at a depth when the σ_{xx}^{dyneq} component of stress approaches σ_{xz}^{static}, as seen in equation (3.21). We refer to this equation to calculate the depth of shear failure with the same parameters as the S-wave example, except a slope angle of 26°, and $a_x = 0.3$ m/s^2. Here, a_z provides the dominant contribution to the PGA of 0.1 g. This analysis gives a depth of $z \approx 3.0$ m.

When normalized to the same PGA, dynamic stress produced by the P-wave is smaller than by the S-wave, especially the σ_{xx}^{dyneq} component. Therefore, as static stress increases, dynamic stress has less influence on the total stress field at a shallower depth than for the S-wave. This is why the S-wave produces shear failure at a greater depth than does the P-wave. Nonetheless, we conclude that each mechanism of failure occurs in the same depth region due to either a P- or S-wave.

3.7 Comparison of Failure due to P- and S-Waves

In nature, when a P-wave passes through a slope, a subsequent S-wave will follow containing larger ground motion amplitude than the P-wave. Therefore, it is the S-wave which is most important for causing failure. But regardless of the type of incoming plane wave, either P or S, both tensile and shear mechanisms of failure take place in a homogeneous slope. This only occurs when there is cohesion in the slope and the incidence of the incoming wave is non-zero.

This analysis also indicates that the depth of failure for an S-wave is similar to that of a P-wave. Tensile failure is produced due to the $\sigma_{xx}^{dynamic}$ component of stress, where the depth of failure relies heavily on cohesion. It is at the near-surface when this component of stress is approximately equal to the tensile strength of the slope and creates tensile failure. While at greater depth, shear failure takes place and the depth of failure relies on the ground motion produced by the incoming wave. Now that a homogeneous slope has been extensively studied, a more realistic scenario represented by a layered slope is outlined in the following chapter.

Chapter 4

LOW VELOCITY LAYER

We now focus attention on the failure mechanisms produced in a slope consisting of a layered medium. Reid & Iverson (1992) verify that a layered slope is a typical phenomenon found in the field:

> "Most natural hillslopes are composed of stratified earth materials with different physical properties. This stratification, resulting from diverse geologic processes, can take many forms, including slope-parallel surficial deposits or weathering layers overlying rock."

With many ways to characterize a layered slope, Terzaghi *et al.* (1996) specify a simple two-layer medium consisting of an upper layer representing a weak, weathered zone of variable thickness overlying rock, usually parallel to the slope surface. Because weathering is largely confined to the upper meters of the slope, this produces a region of lower strength and, thus, an area more prone to slope failure than the underlying sedimentary layer (Selby, 1993). In many cases, the sedimentary layer is less permeable than the overlying, weathered layer. When pore-fluid from rainstorms passes through the weathered layer, it is unable to penetrate the less permeable layer below and builds at the interface between the two layers, creating a zone of weakness. This is what is thought to have caused the La Conchita, California landslide in January, 2005 (Figure 4.1) (Jibson, 2005). Massive rainstorms soaked Southern California creating widespread saturation and the potential for landslides. By the time

Figure 4.1. Site of the La Conchita, California landslide of January, 2005. This landslide was caused by massive rainstorms which soaked Southern California that winter (from Godt & Reid, 2005).

the slope failed, the upper layer was actually dry, not saturated as it was thought to be. Pore fluid became trapped at an interface below the surface creating a failure plane for the slide to eventually take place.

Following the description of a layered slope by Terzaghi *et al.* (1996), we focus on the failure analysis of an unsaturated, two-layer slope where the shallow upper meters represent a low velocity, weathered layer that overlies a stronger, sedimentary layer. Figure 4.2 is a schematic of the model used in this analysis, represented by a welded interface. The low velocity layer, 5 meters deep, contains parameters α_1, β_1, ρ_1, ϕ_1 and c_1 that are less than those for the sedimentary layer, α_2, β_2, ρ_2, ϕ_2 and c_2. Parameters of the upper layer represent unconsolidated sediments similar

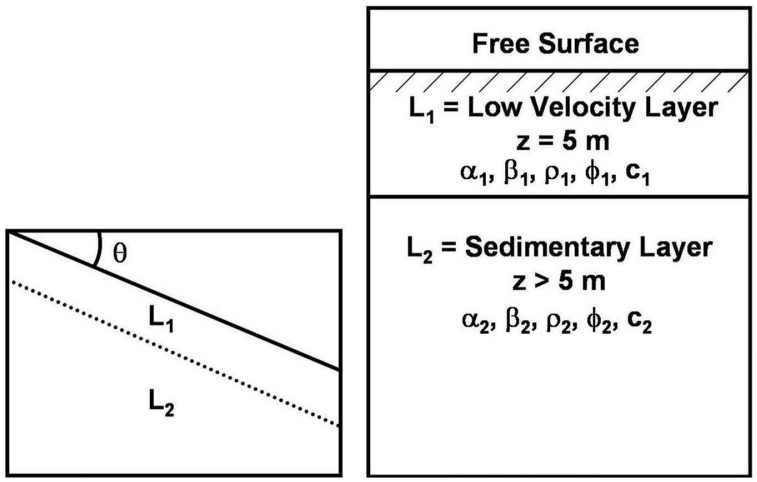

Figure 4.2. Layered model describing depths and parameters for each layer created in this study.

to those modeled in the homogeneous slope and the lower layer contains parameters representing rock, stronger than the upper layer and homogeneous slope. We test variable strength parameters in each layer to see which produce greater regions of failure as compared to the homogeneous model.

Before sending a plane wave through this layered slope, a static stress analysis is completed to test for failure of each layer in the static slope. Therefore, during the dynamic analysis, the incoming wave causes failure at shallower slope angles.

4.1 Dynamic Analysis

The goal of this analysis is to see how a slope consisting of both strong and weak layers can alter the failure mechanisms that occur in a homogeneous slope. It is possible that this model may produce locations of failure at or near the interface between layers of variable strength. It could also be the case that the shallow layer has little impact on slope stability.

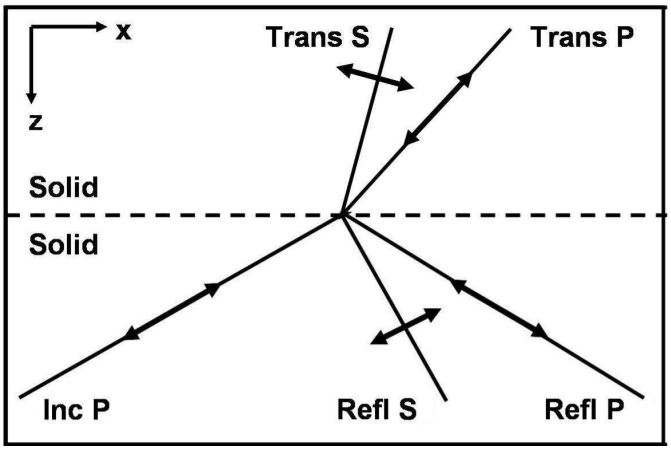

Figure 4.3. Incident P-wave on a solid/solid interface producing reflected and transmitted P- and S-waves. The arrows indicate the direction of wave motion (modified from Haney, 2004).

The interface between the two layers represents a solid/solid boundary. An incoming wave that hits this interface produces a different set of reflected and transmitted waves than for the homogeneous model. Figure 4.3 shows how an incident P-wave behaves at this boundary. Unlike the homogeneous model, this incident wave produces two transmitted waves in the upper layer which strike the free surface, while two reflected waves are produced at the boundary and propagate into the lower layer. The surface of the low velocity layer represents the free surface of the slope. Once the transmitted waves in this layer make contact with the surface, they produce additional reflected P- and S-waves, as seen in Figure 3.2. Because of Snell's law, the horizontal slowness of the incident wave remains the same while crossing the interface between layers during the reflection/transmission process (Aki & Richards, 2002). Because the upper layer has velocities less than the sedimentary layer, the angles of the transmitted waves are less than the reflected P- and S-wave.

Previously demonstrated, the dynamic stress generated by an S-wave is larger

Model	α	β	ρ	ϕ	c
Homogeneous	1730 m/s	500 m/s	2000 kg/m^3	32°	10 kPa
Layered: Low Velocity	1500 m/s	800 m/s	1500 kg/m^3	32°	10 kPa
Layered: Sedimentary	2200 m/s	1000 m/s	2200 kg/m^3	40°	50 kPa

Table 4.1. Values used in each type of slope model. In the layered model, the low velocity layer contains parameters smaller than the stronger, sedimentary layer.

than for a P-wave. Again, a 30° incident S-wave normalized to a PGA of 0.1 g is used in this analysis. The parameters used in the layered and homogeneous models are shown in Table 4.1. For the homogeneous case, parameters represent soil in a slope. This is the first step to understanding failure in a constant medium, without having to model fractures that occur in stronger material such as rock. The upper, weathered layer in the layered model also represents weak, unconsolidated soil and is created using parameters similar to those for the homogeneous model. We use the same strength parameters for both the homogeneous model and weathered layer so we can see how failure compares in the upper meters of the slope, where tensile failure tends to occur.

Because different parameters are used between the homogeneous and layered models, the dynamic stress produced in each model is also different. To understand the difference in dynamic stress, we analyze the dynamic stress equations (3.10-3.12). The layered model produces larger stress than the homogeneous model when using equation (3.12) to calculate σ_{xx}^{dyneq} at the surface of the slope. This is because the S-wave velocity for the layered model at the surface is larger than the homogeneous slope, as shown in Table 4.1. Additionally, all dynamic stress components for the layered model are comparable or larger than the homogeneous slope for depths of 1 m and 6 m, representing both weathered and sedimentary layers.

Overall, given the difference in dynamic stress and the parameters outlined in Table 4.1, the mechanisms of failure indicated for a layered slope are the same as the homogeneous model. With the S-wave normalized to a PGA of 0.1 g, the layered slope produces tensile failure at the surface and shear failure in both upper and lower layers at depth.

The thickness of the upper layer, only 5 m deep, is a fraction of the wavelength of the incoming wave, which is 800 m for a frequency of 1.0 Hz. Because the wavelength is much larger than the depth of this layer, the weathered layer has little impact on creating additional locations of slope instability and failure in the layered slope ultimately resembles that in the homogeneous model.

Since the dynamic stress is larger than for the homogeneous case, failure takes place at shallower slopes. The first instance that both shear and tensile failure take place in the layered medium is for a slope of 19°, while statically, failure for the entire slope occurs at 40°. The principal stresses for this 19° slope in Figures 4.4-4.5, show that, generally, the stress for the layered model is similar to that in the homogeneous case. Again, tensile stress is produced at the near-surface, while compressional stress is dominant at depth. For the layered slope, tensile stress exists at a greater depth than for the homogeneous case, although below 1 m, is not large enough to generate tensile failure.

Figures 4.6 and 4.7 display the stress difference to both tensile and shear failure for the layered slope with the interface marked at 5 m depth. There are two distinct locations of failure, each providing a different mechanism of failure. The weathered layer is initially failing in a tensile manner near the surface up to 1 m depth, while the remainder of the layer does not fail. Below the interface, the only indication of failure is at 6 m depth, which is in shear.

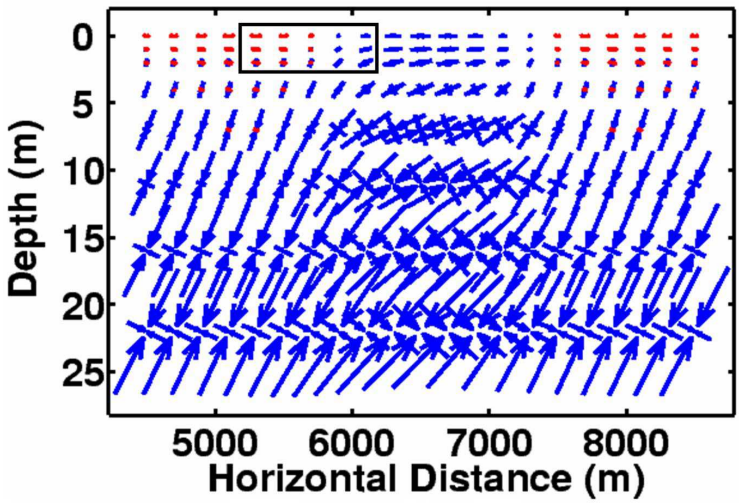

Figure 4.4. Principal stress components and directions computed for a 19° layered slope due to a 30° incident S-wave normalized to a PGA=0.1 g. The interface between the two layers lies at 5 m. The box is enlarged in Figure 4.5 to show the detail of tensile stress produced in this model.

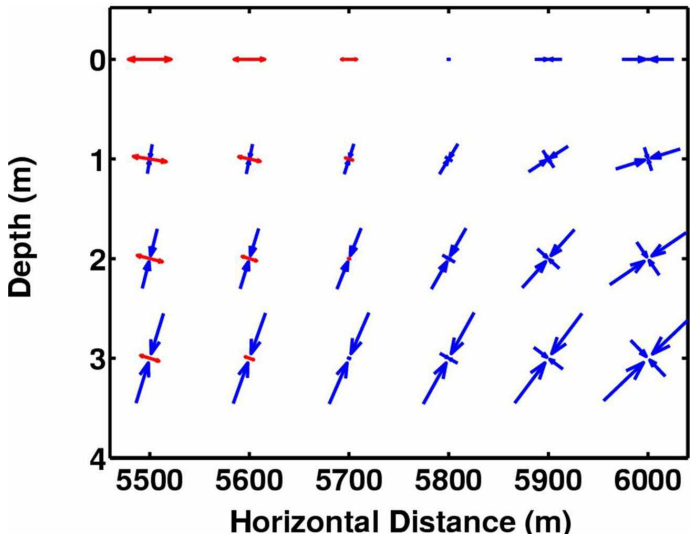

Figure 4.5. Enlarged image from Figure 4.4 showing both regions of extensional and compressional stress at the surface. Here, extensional stress leads to tensile failure in the near surface. Tensile stress exists at a greater depth than previously seen, although, at depths greater than 1 m, tensile failure does not take place.

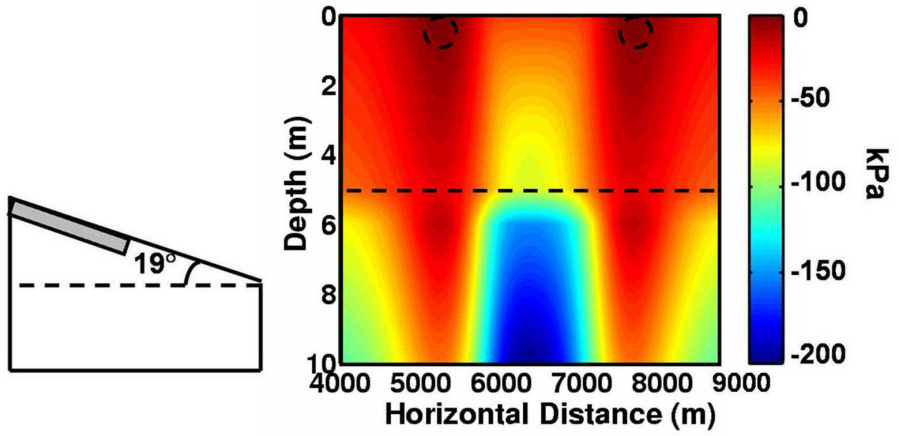

Figure 4.6. In the right panel, the stress difference to tensile failure is displayed for a layered slope of 19° and $c = 10$ kPa due to a 30° incident S-wave normalized to a PGA=0.1 g. The boundary between the two layers is indicated by the dotted line. The shaded area in the left panel indicates the region of the slope shown on the right. Failure occurs at the near surface, indicated by the circled regions.

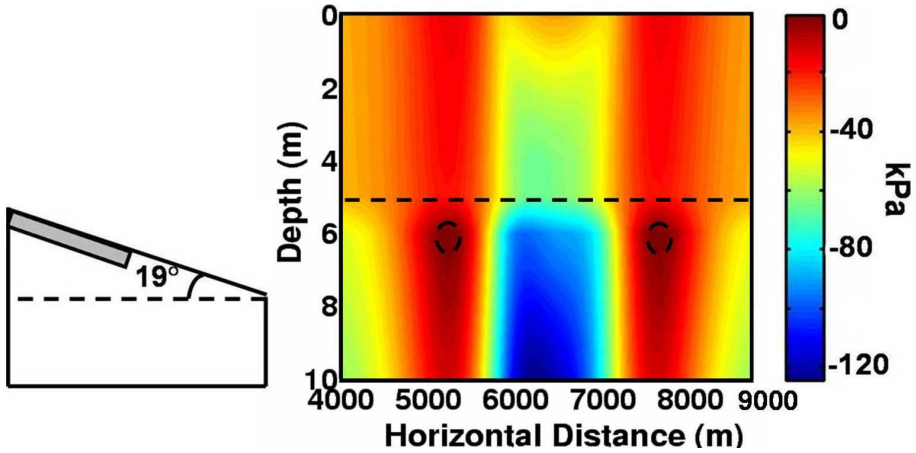

Figure 4.7. In the right panel, the stress difference to shear failure is displayed for a layered slope of 19° and $c = 50$ kPa due to a 30° incident S-wave normalized to a PGA=0.1 g. The boundary between the two layers is indicated by the dotted line. The shaded area in the left panel indicates the region of the slope shown on the right. The initiation of shear failure is circled at 6 m depth.

Because the layered slope contains physical properties that vary with depth, it is impossible to correctly utilize the dynamic stress equations (3.10-3.12) which are a substitute for dynamic stress in the homogeneous slope. Because of variation in stress with depth, these equations become insufficient approximations.

This analysis concludes that, regardless of the type of slope, failure due to the layered model occurs in the same manner as the homogeneous slope. As seen from the principal stresses in Figure 4.5, at the near surface $\sigma_{xx}^{dynamic}$ is the dominant contribution for tensile failure. Shear failure also takes place at depth. This is a depth at which static stress becomes large enough that when combined with $\sigma_{xx}^{dynamic}$, failure takes place in a shear manner. Below this depth, as σ_{zz}^{static} increases with respect to $\sigma_{xx}^{dynamic}$, failure no longer takes place in the slope.

Now that we've taken the time to determine failure for various unsaturated slopes, in the next chapter, we explore slope instability in a deep-water environment where overpressure is the dominant factor in causing slope failure.

Chapter 5

OVERPRESSURE

Previous chapters outlined the failure mechanisms for slopes consisting of unsaturated soils. Another pressing issue for landslide hazards involves overpressure layers in deep water environments, which cause failure of submarine slopes and extensive costs to the petroleum industry. This chapter reviews this phenomenon and how the stress model can be used to understand slope instability for this type of environment.

For unsaturated soils, voids between particles, or pore spaces, are filled with air and the pore-fluid pressure is essentially equal to zero. When sediments are exposed to a deep water environment, as ocean sediments are, pore spaces are saturated with fluid, creating the potential for pore pressure induced submarine slides to occur. This is a problem affecting the petroleum industry, which is expanding operations into deeper waters. Therefore, it is important to understand the stability of submarine slopes before companies attempt to drill in these areas (Sparkman, 2002).

Consolidated soils have a normal stress equal to the weight of overlying sediments (Middleton & Wilcock, 1994). This stress, which increases linearly with depth, is known as lithostatic pressure (Turcotte & Schubert, 2002). When pore fluid is drained out of sediments during consolidation, the pore pressure is equal to hydrostatic. The lithostatic and hydrostatic pressures are defined as:

$$P_{lithostatic} \approx \rho_{rock} g z \ , \tag{5.1}$$

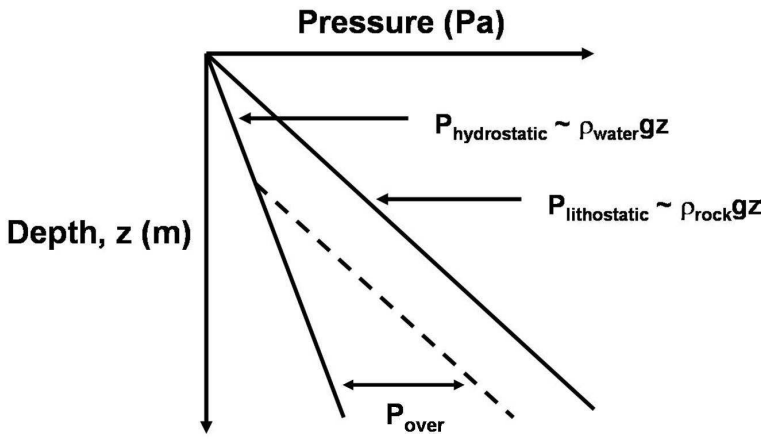

Figure 5.1. Lithostatic and hydrostatic pressures as a function of depth, as well as how overpressure, P_{over}, is the pressure in excess of hydrostatic (modified from Ostermeier *et al.*, 2002).

$$P_{hydrostatic} \approx \rho_{fluid} g z \ , \tag{5.2}$$

where g is gravitational acceleration and z, depth.

In cases of rapid consolidation, pore space between particles is reduced and pore fluid is unable to drain. Water can become trapped and cause pore pressure to build. Areas where pore pressure increases in excess of hydrostatic pressure are known as geopressure or overpressure zones (Middleton & Wilcock, 1994). Figure 5.1 displays how hydrostatic and lithostatic pressures behave with depth. Lithostatic pressure is larger than hydrostatic pressure due to the density of rock being larger than that of fluid. The overpressure, P_{over}, is defined as the pressure greater than hydrostatic. Overpressure is known to exist in deep water near the seabed and increase with depth, up to 1,200 m below mudline (Ostermeier *et al.*, 2002).

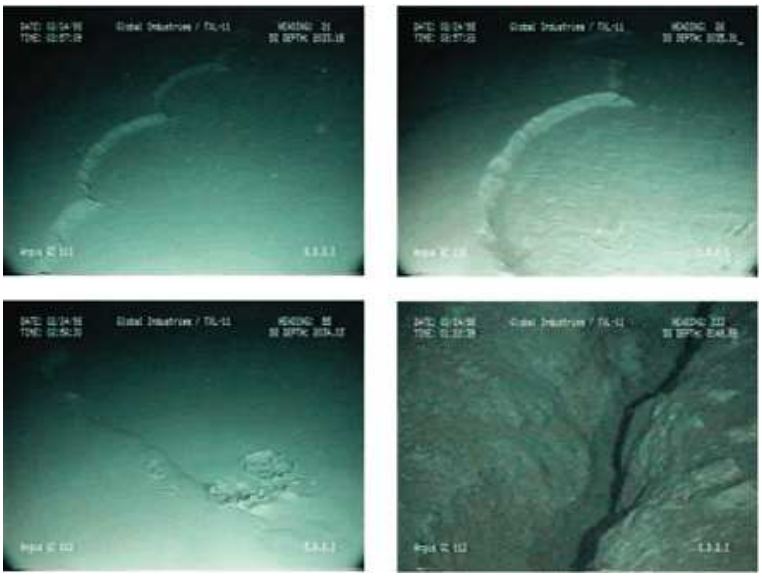

Figure 5.2. Shallow water flows created by overpressure in the Gulf of Mexico (from Ostermeier *et al.*, 2002).

5.1 Shallow Water Flows and Detection of Overpressure

Shallow water flows (SWF) are submarine landslides caused by internal failure due to overpressured sands and low formation strength in water deeper than 600 ft (Sparkman, 2002). Although taking place in deep water, shallow water flows are relatively shallow in depth below the mudline. Figure 5.2 shows images of shallow water flows in the Gulf of Mexico. There is disruption along the sea floor due to turbidite flows as well as cracks and fissures created in the rock (Ostermeier *et al.*, 2002).

SWF take place when drilling into poorly consolidated overpressure layers and pose a threat to drilling safety in deep water. These flows can cause major damage to a bore hole and well site leading to the possibility of lost wells. Approximately 70% of all deep-water wells in the Gulf of Mexico have experienced shallow water

flows at some point (Dutta *et al.*, 2002). This problem is a major concern in other deep-water locations around the globe such as the Mediterranean, and coasts off Nigeria and Brazil. Costs to industry associated with overpressure failure are nearly $1 billion per year worldwide (Dutta *et al.*, 2002). Therefore, estimating the locations of overpressured zones prior to drilling is essential to minimize hazards and costs. Currently, most overpressure data are collected from the Gulf of Mexico (Mukerji *et al.*, 2002).

Anomalously high pore-pressure zones are commonly associated with altering geophysical properties, such as the lowering of seismic velocities (Dutta *et al.*, 2002). Typically, compressional and shear velocities in crustal rocks increase with confining pressure. The effect of pore pressure is to counteract that of confining pressure by propping open pore space. High pore pressure then tends to lower velocity (Dutta *et al.*, 2002). Because pore fluid does not support shear-wave propagation, higher pore pressures cause a greater reduction in S-wave velocity then for P-wave velocity (Lee, 2003).

Reflection seismic methods are used for predicting high pore pressures, exploiting the fact that overpressure intervals have velocities lower than those in normally-pressured layers at the same depth. By obtaining this information through seismic imaging, it is possible to locate layers of trapped fluid and, therefore, zones of overpressure (Dutta *et al.*, 2002). Even with the techniques already employed to help detect overpressure prior to drilling, there is no single method that can predict every occurrence of overpressure (Mukerji *et al.*, 2002).

5.2 Causes of Overpressure

Overpressure can occur due to a variety of natural processes such as undercompaction, fluid expansion, lateral transfer and tectonic loading, any combination of which has the potential to create high pore pressures (Bowers, 2002).

Undercompaction is rapid sedimentation with the potential to bury large amounts of sediments and prevent pore fluid from draining, making overpressure possible. Excess pressure builds as the weight of overlying sediment increases and squeezes fluid through low permeability sands and clays creating higher pressure (Bowers, 2002). In the Gulf of Mexico, overpressure is mainly caused by rapid sedimentation (Prasad, 2002).

Fluid expansion involves fluids that expand during chemical reactions near the seafloor. Pore fluid increases in volume due to these circumstances, causing excess pressures (Bowers, 2002). In a manner similar to fluid expansion, it is also possible for pore fluid to be pumped into sealed intervals from higher pressure layers creating overpressure zones due to lateral transfer. This can occur by fluid moving along faults or when a dipping higher permeable sand is enclosed by a lower permeable shale. In this case, pore fluid is transfered updip from the sand into the shale (Bowers, 2002).

Also similar to lateral transfer, tectonic loading occurs when pore fluid is squeezed by tectonically driven stresses through rock to induce overpressure. This loading of pressure is related to normal or thrust type faulting (Bowers, 2002).

Due to the variety of potential overpressure causes, it is important to adopt techniques for locating these intervals and understand how they affect submarine slope stability. Therefore, the stress model is used to detect stability of submarine slopes when high pore pressures are present and to understand the circumstances creating failure.

5.3 Modeling Submarine Slope Stability and Overpressure

Terzaghi's effective stress principle helps to understand the effects of pore pressure in the stress model. Because shear stress is unaffected by pore pressure, effective normal stress is equal to the total normal stress minus pore pressure (Terzaghi *et al.*, 1996). In the stress model, overpressure acts as the pore pressure greater than hydrostatic pressure,

$$\sigma'_{ij} = \sigma_{ij} - P_{over}\delta_{ij} \ . \tag{5.3}$$

The Mohr-Coulomb criterion, which is used to estimate shear submarine failure, utilizes the concept of effective stress (Middleton & Wilcock, 1994),

$$\tau = c + \sigma' \tan(\phi) \ . \tag{5.4}$$

When constructing the Mohr circle of stress including pore pressure, this pressure is subtracted from the principal stress components, σ_1 and σ_3, which has no affect on the radius of the circle (Middleton & Wilcock, 1994). As seen in Figure 5.3, as pore pressure is increased, the effective stress is reduced and the Mohr circle moves to the left until it touches the envelope causing failure. By incorporating parameters of deep-water sediments and pore pressure, we model submarine slope stability. This helps to explain how close certain marine sediments containing overpressure may be to failure.

The first test provides the stability of a homogeneous, 32° slope analyzed at hydrostatic pressures, where overpressure is zero. The slope is comprised of weakly consolidated sediments with density, $\rho = 2,000$ kg/m^3. The cohesive values for rock are much larger than for the soils used in the previous study. For a sedimentary rock such as sandstone or shale, cohesion can range from 1-20 MPa while friction angles

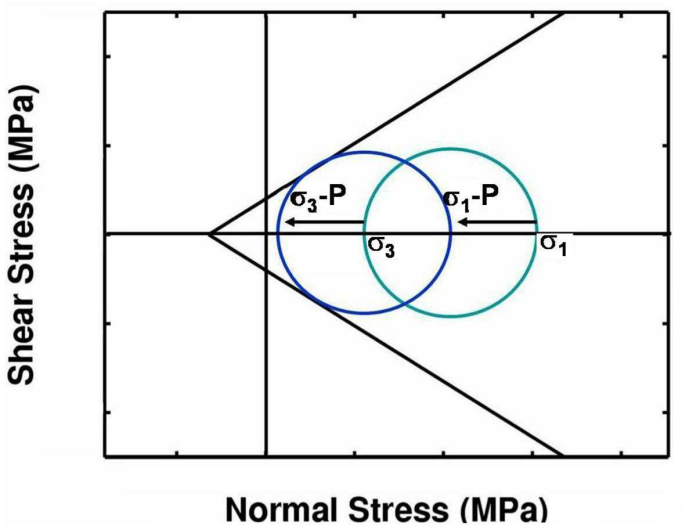

Figure 5.3. The Mohr circle of stress affected by pore pressure (modified from Middleton & Wilcock, 1994).

may range from 25°-35° (Selby, 1993). For this analysis, $c = 2$ MPa and $\phi = 32°$. The λ and μ values used to calculate σ_{xx}^{static} are based on $v_p = 2,000$ m/s and $v_s = 500$ m/s.

By analyzing this slope at a depth of 200 m below mudline, the Mohr circle produced in Figure 5.4 displays a stable layer. In this example, the stability of the slope is calculated without overpressure, allowing measurement of the critical overpressure necessary to drive the slope to failure. The critical overpressure, P_{crit}, is found by measuring the normal stress between the top of the Mohr circle horizontally across to the failure envelope. The critical overpressure to create failure in this slope is 2 MPa.

Figure 5.5 shows the stability of the slope after 2 MPa of overpressure has been applied to this model. The effective stress is reduced, and now the Mohr circle touches the failure envelope. Given the P_{crit} calculated from Figure 5.4, this provides

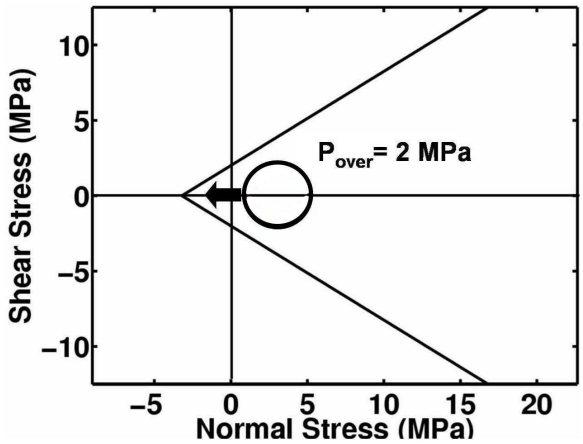

Figure 5.4. Mohr-Coulomb failure analysis for a layer of sediment at 200 m below mudline and a slope of 32°. The arrow indicates how much overpressure is necessary to cause failure, measured as 2 MPa.

the analysis of how the slope is expected to behave. According to Prasad (2002), this is an average value for overpressure given the depth and velocities used in this model.

We now examine the potential for failure given an unstable slope due to pore-pressure. Beginning with the statically stable slope shown in Figure 5.4, 1.5 MPa of overpressure in included to produce the Mohr circle shown in Figure 5.6. The Mohr circle is not touching the failure envelope, but is closer to failure than without the added pressure. There is not much additional stress the slope can withstand before failure takes place. Assuming this represents a slope in the Gulf of Mexico or other deep-water drilling location, additional stress can come from drilling in the area, or from seismicity.

With this in mind, a 30° incident P-wave normalized to a PGA of 0.1 g is sent through this slope to monitor how the stability of the overpressured slope changes.

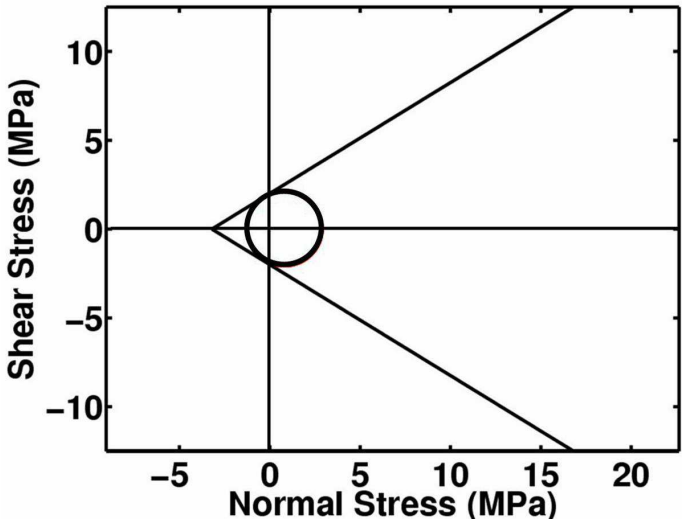

Figure 5.5. Mohr-Coulomb failure analysis for a layer of sediment at 200 m below mudline and a slope of 32° including 2 MPa of overpressure. The circle indicates failure has occurred at this location.

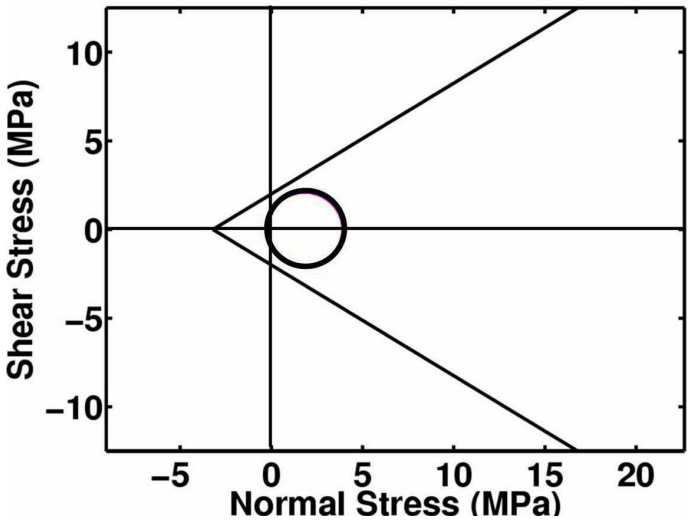

Figure 5.6. Mohr-Coulomb failure analysis for a layer of sediment at 200 m below mudline and a slope of 32° with 1.5 MPa of overpressure. This produces a circle close to failure and a case of instability.

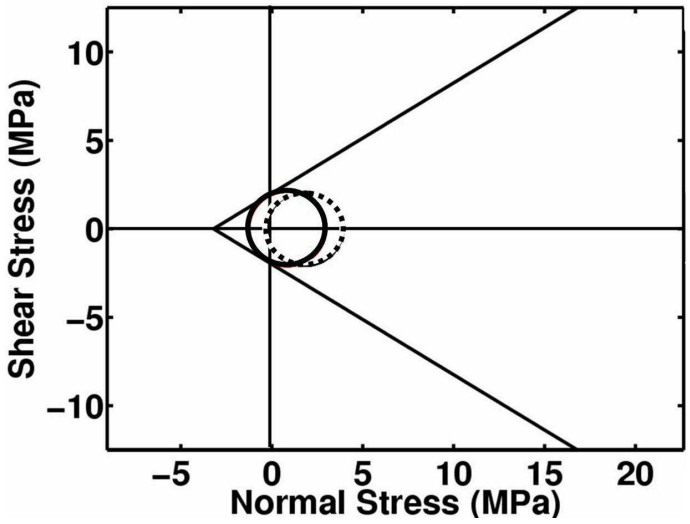

Figure 5.7. Mohr-Coulomb failure analysis for a layer of sediment at 200 m below mudline and a slope of 32° with 1.5 MPa of overpressure. This layer has been exposed to a 30° incident P-wave normalized to a PGA=0.1 g, which causes the unstable overpressure layer (dotted circle) to fail (solid circle).

Figure 5.7 shows this incoming wave has a dynamic stress large enough to cause the static layer, represented by the dotted Mohr circle, to fail, shown as the solid Mohr circle. Note that the solid circle is slightly larger because this Mohr circle is produced with both static and dynamic stress, creating larger shear and normal stresses. A slope containing overpressure influenced by dynamic stress is more susceptible to failure than a slope that has not been subjected to seismicity. This analysis indicates that small dynamic disturbances such as seismicity, induced seismicity from hydrocarbon production and disturbances from drilling can produce enough stress to cause an overpressured layer to fail.

5.4 Overpressure Analysis

Slope-stability analysis is an important topic to pursue both above and below water. Overpressure has become an increasingly hazardous and expensive problem for the petroleum industry. This is why Orange *et al.* (2003) state that proper modeling of pore pressure is crucial for assessing the stability of submarine slopes. Even though these tests are only carried out for a homogeneous slope, our stress model provides a simple test and basic understanding of slope stability due to overpressure. This analysis, along with the help of reflection seismic methods and other acoustical and rock property measurements have the potential to make for proper precautions against shallow water flow hazards.

Chapter 6

DISCUSSION

The dynamic stress generated by earthquakes is one of the significant causes for triggering landslides, one of the many damaging hazards on Earth. It is important to understand the mechanism of how such landslides form and ultimately how failure is triggered in susceptible slopes. The goal of this project is to describe the role of shear and tensile failure in the triggering of landslides. Our model provides evidence for the initiation of both types of failure in a slope subject to dynamic stress.

6.1 Collaboration of Shear and Tensile Failure

In this thesis, we discuss the limit-equilibrium model used to investigate dynamic stress associated with ground motion in a slope. This analysis provides examples showing how tensile failure occurs in the upper meters of a slope due to dynamic stress, $\sigma_{xx}^{dynamic}$, and at depth, shear failure takes place.

To further understand the regions of shear and tensile failure in a slope, dynamic stress equations are derived that relate dynamic stress to the acceleration at the surface of a slope. By specifying the PGA in this analysis, these equations produce dynamic stress as a function of depth and help to define the depth of each mechanism of failure. The depth of tensile failure depends on the tensile strength of the slope. Because this mechanism of failure does not depend on slope angle, it is possible for tensile cracks to form at the surface of a horizontal slope, like those shown in Figure 1.4. The approximate depth of shear failure depends on the ground motion produced

by an incoming wave.

King & Sammis (1992) state that complex failure involves the interaction between simple processes occurring on a wide range of scales. With two separately defined depths for shear and tensile failure outlined in this project, we believe that the two failure mechanisms collaborate and eventually cause slope failure. Since this project focuses on a limit-equilibrium method, we cannot model displacement of a slope, but can speculate about the role of shear and tensile failure in the deformation process.

Laboratory experiments of rock failure are known to produce three mechanisms of failure; shear and splitting in compression as well as tensile failure (Scholz, 2002). In compression tests, small-scale samples fail entirely in shear. This process cannot occur for large-scale structures, such as slopes, because failure would extend indefinitely through the Earth. This is why King & Sammis (1992) propose that shear failure must initiate due to the underlying process of tensile failure. Figure 6.1 displays a schematic of how shear failure is thought to form in these rock samples. The initiation of shear failure results from small regions of tensile failure at the ends of the crack produced. The crack along which shear failure exists grows until the entire sample fails in shear. Therefore, shear failure in rock ultimately results from the collaboration of both shear and tensile failure.

As seen in the field, failure at one scale leads to failure at another scale in a process of evolving damage (King & Sammis, 1992). So, if small tensile cracks are formed in the process to create shear failure as seen in Figure 6.1, then it is not uncommon to see large scale tensile deformation in the displacement of a slope. With this information, Figure 6.2 is created to show the depths indicated by the model for each type of failure mechanism. Due to dynamic stress, the upper meters of the slope tend to be in a state of extension, leading to tensile failure, noted in red. At greater

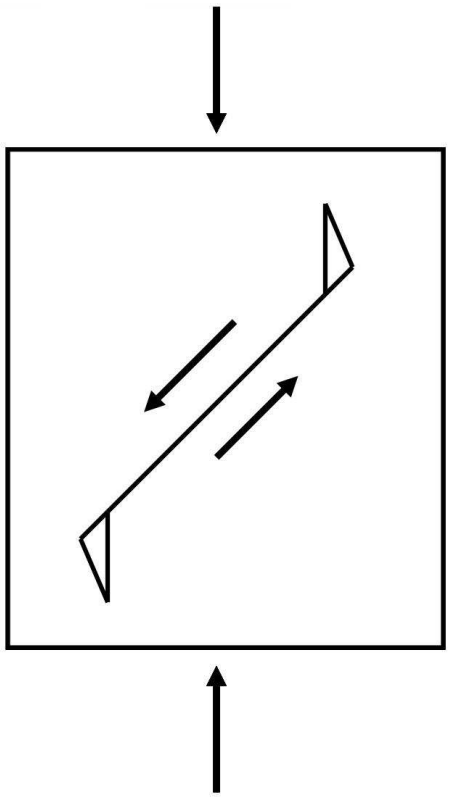

Figure 6.1. Compression test creating shear failure in a rock sample. The initiation of shear failure results from the creation of tensile failure at the tips of the crack. The crack along which shear failure exists grows until the entire sample fails in shear (modified from King & Sammis, 1992).

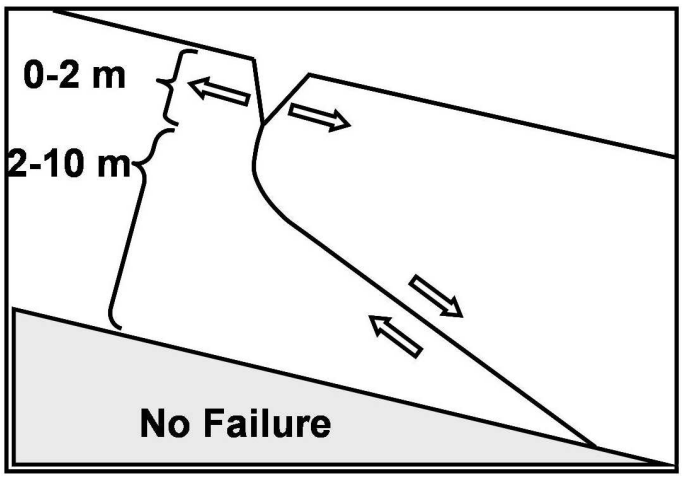

Figure 6.2. Combining the two mechanisms of failure indicated by the model and how they work together to create slope deformation. When both failure mechanisms exist in a slope, they do not take place at the same location. Tensile failure near the surface is shown in red, while the blue region refers to shear failure, below which, failure will not occur.

depths, shear failure takes place up to a finite depth, such as 10 m for example, shown in blue. Below this depth, failure does not take place. From this figure, it becomes clear that both failure mechanisms work together to cause landslides. Stress concentrations build as the first mechanism of failure initiates, inducing the second failure mechanism to occur. We are unable to determine from this model which type of failure occurs first in a slope and at what point displacement takes place. These figures help link how the shear and tensile failure mechanisms produced from the model can actually occur in nature.

6.2 Future Work

This stress model takes a step further to investigate limit-equilibrium of a slope due to dynamic stress. Because the tests described here are the first analyzed, there

are potential areas for improvement to make this model more widely applicable.

The static stress produced for this model is introduced in Chapter 3. As discussed, the critical angle at which static stress produces failure is less than traditional limit-equilibrium methods. This in turn causes dynamic failure to occur at shallower slope angles. One aspect for future work would be to research how other static stress models, such as those outlined in Savage & Smith (1986) and Savage & Swolfs (1992), may change the slope angle at which failure occurs.

Further, the 1D wave equation code used in this model only provides the opportunity to work with plane waves. As the first stage in this analysis, this is useful for understanding the failure process. However, these are not the only types of waves produced from an earthquake source. Surface waves have the potential to create destructive dynamic stress at the surface of a slope before they attenuate with time. By combining this with the stress produced from plane waves, it is possible that slopes become more susceptible to a particular mechanism of failure.

We also realize that earthquake magnitude, distance of the incoming wave and duration of shaking can have a strong influence on the amount of damage produced, which is not taken into consideration for this project. Additionally, actual earthquake data are not examined in the stages of this project, such as Newmark's method does. This would allow us the opportunity to analyze if actual ground motion data provide the same results of failure as those in this project. The next step for this research should incorporate these additional dynamic scenarios.

Although a limited number of likely slope situations is tested, it would be impossible to analyze each type of slope at this preliminary stage. The tests which have been completed give a general understanding of failure. There are many properties that were not included in this model which may produce a more realistic slope sce-

nario, such as inhomogeneous materials including clay, rocks and boulders and even slopes comprised of more than two sedimentary layers. Regardless of the number of slope tests that could be completed, the contributing factor to shear and tensile failure in the slope comes from $\sigma_{xx}^{dynamic}$ due to the incoming wave. Therefore, it is likely that these conditions will not change the outcome of failure, but will change the strength of the slope and the slope angle at which failure occurs.

One important property in Chapter 5, is pore pressure. Even though only a few tests are described for overpressured slopes, we understand how pore pressure influences failure in a slope. If pore pressure is introduced into either the homogeneous or layered slope model, the effective stress in the slope would be reduced, causing shear and tensile failure to occur more quickly. So, without testing explicitly for this property, we acknowledge the basic outcome.

6.3 Contribution to Landslide Hazards

It is imperative that we continue to monitor landslide hazards and provide a better understanding of how and why they occur. This project provides an additional viewpoint about the manner in which particular earthquakes cause slope failure. Given particular slope information we can test the susceptibility to both shear and tensile failure due to varying dynamic stress.

This stress model is a significant contribution to those interested in landslide hazards such as geoscientists, engineers and developers, providing the ability to better understand how slope deformation takes place given initiation of shear and tensile failure. More importantly, this may be used to help prevent development of communities near earthquake-prone slopes.

Another way to increase knowledge about the potential danger of landslides and earthquakes is through hazard mapping. This model can help contribute to the creation of landslide susceptibility maps for locations prone to earthquake hazards. This means that federal, state and local governments can create and use these maps with more precision by understanding the different failure mechanisms possible.

Further, this work may help to better methods which are currently in use. This could lead to changes in these methods by incorporating ways to measure tensile failure in addition to shear failure, as well as monitoring the dynamic stress produced from an earthquake. This project provides valuable insight into the generation of slope failure and will help to create a more complete dynamic model. We wish for this information to help guide landslide mitigation efforts to reduce these devastating hazards.

REFERENCES

Aki, K., & Richards, P. G. 2002. *Quantitative Seismology, Second Edition*. University Science Books.

Bourne, S. J., & Willemse, E. J. 2001. Elastic Stress Control on the Pattern of Tensile Fracturing Around a Small Fault Network at Nash Point, UK. *Journal of Structural Geology*, **23**, 1753–1770.

Bowers, G. L. 2002. Detecting High Overpressure. *The Leading Edge*, feb, 174–177.

Brace, W. F. 1960. An Extension of the Griffith Theory of Fracture to Rocks. *Journal of Geophysical Research*, **65**(10), 3477–3480.

Committee on Ground Failure. 1985. *Reducing Losses From Landslides in the United States*. Committee on Ground Failure Hazards, Washington, D.C.

Das, B. M. 1997. *Advanced Soil Mechanics, Second Edition*. Taylor and Francis.

Dutta, N., Mukerji, T., Prasad, M., & Dvorkin, J. 2002. Seismic Detection and Estimation of Overpressures, Part II: Field Applications. *CSEG Recorder*, september, 58–73.

Evans, S. G., & Bent, A. L. 2004. The Las Colinas Landslide, Santa Tecla: A Highly Destructive Flowslide Triggered by the January 13, 2001, El Salvador Earthquake. *Natural Hazards in El Salvador: Geological Society of America Special Paper*, **375**, 25–38.

Frankel, A. D. 1999. Earthquake Ground Motion: How Does the Ground Shake? *Science*, **283**(5410), 2032–2033.

Godt, J., & Reid, M. 2005. *Aerial Reconnaissance of Landsliding in Southern California, 2005*. World Wide Web. http://landslides.usgs.gov/.

Haney, M. M. 2004. *An Investigation of Sealing and Episodic Pulsing of Fluids at a Minibasin-Bounding Growth Fault from Seismic Reflection Images*. Ph.D. thesis, The Colorado School of Mines.

Harp, E. L., & Jibson, R. W. 1995. Seismic Instrumentation of Landslides: Building a Better Model of Dynamic Landslide Behavior. *Bulletin of the Seismological Society of America*, **85**(1), 93–99.

Iverson, R. M., & Reid, M. E. 1992. Gravity-Driven Groundwater Flow and Slope Failure Potential 1. Elastic Effective-Stress Model. *Water Resources Research*, **28**(3), 925–938.

Jaeger, J. C., & Cook, N. G. 1976. *Fundamentals of Rock Mechanics*. John Wiley and Sons, Inc.

Jibson, R. W. 1993. Predicting Earthquake-Induced Landslide Displacements Using Newmark's Sliding Block Analysis. *Transportation Research Record*, **1411**, 9–17.

Jibson, R. W. 2005. *Landslide Hazards at La Conchita, California*. Tech. rept. U. S. Geological Survey Open-File Report 2005-1067.

Jibson, R. W., & Crone, A. J. 2001. *Observations and Recommendations Regarding Landslide Hazards Related to the January 13, 2001 M-7.6 El Salvador Earthquake*. Tech. rept. U. S. Geological Survey Open-File Report 01-0141, http://pubs.usgs.gov/of/2001/ofr-01-0141/.

Jibson, R. W., Harp, E. L., & Michael, J. A. 2000. A Method for Producing Digital Probabilistic Seismic Landslide Hazard Maps. *Engineering Geology*, **58**, 271–289.

King, G. C., & Sammis, C. G. 1992. The Mechanisms of Finite Brittle Strain. *Pure and Applied Geophysics*, **138**(4), 611–640.

Konagai, K., Johansson, J., Mayorca, P., Uzuoka, R., Yamamoto, T., Miyajima, M., Pulido, N., Sassa, K., Fukuoka, H., & Duran, F. 2004. Las Colinas Landslide: Rapid and Long-Traveling Soil Flow Caused by the January 13, 2001, El Salvador Earthquake. *Natural Hazards in El Salvador: Geological Society of America Special Paper*, **375**, 39–54.

Lee, M. W. 2003. *Elastic Properties of Overpressured and Unconsolidated Sediments*. Tech. rept. U. S. Geological Survey Bulletin 2214.

Mello, U. T., & Pratson, L. F. 1999. Regional Slope Stability and Slope-Failure Mechanics from the Two-Dimensional State of Stress in an Infinite Slope. *Marine Geology*, **154**, 339–356.

Middleton, G. V., & Wilcock, P. R. 1994. *Mechanics in the Earth and Environmental Sciences*. Cambridge University Press.

Mukerji, T., Dutta, N., Prasad, M., & Dvorkin, J. 2002. Seismic Detection and Estimation of Overpressures, Part I: The Rock Physics Basis. *CSEG Recorder*, september, 34–55.

Newmark, N. M. 1965. Effects of Earthquakes on Dams and Embankments. *Geotechnique*, **15**(2), 139–160.

Orange, D. L., Saffer, D., Jeanjean, P., Al-Khafaji, Z., & Riley, G. 2003. Measurements and Modeling of the Shallow Pore Pressure Regime at the Sigsbee Escarpment: Successful Prediction of Overpressure and Ground-Truthing with Borehole Measurements. *The Leading Edge*, september, 906–913.

Ostermeier, R. M., Pelletier, J. H., Winker, C. D., Nicholson, J. W., Rambow, F. H., & Cowan, K. M. 2002. Dealing with Shallow-Water Flow in the Deepwater Gulf of Mexico. *The Leading Edge*, july, 660–668.

Prasad, M. 2002. Acoustic Measurements in Unconsolidated Sands at Low Effective Pressure and Overpressure Detection. *Geophysics*, **67**(2), 405–412.

Reid, M. E., & Iverson, R. M. 1992. Gravity-Driven Groundwater Flow and Slope Failure Potential 2. Effects of Slope Morphology, Material Properties, and Hydraulic Heterogeneity. *Water Resources Research*, **28**(3), 939–950.

Savage, W. Z., & Smith, W. K. 1986. *A Model for the Plastic Flow of Landslides*. Tech. rept. U. S. Geological Survey Professional Paper 1385.

Savage, W. Z., & Swolfs, H. S. 1992. Near-Surface Crustal Stresses - Theory and Application. *Trends in Geophysical Research*, **1**, 217–250.

Scholz, C. H. 2002. *The Mechanics of Earthquakes and Faulting*. Cambridge University Press.

Selby, M. J. 1993. *Hillslope Materials and Processes, Second Edition*. Oxford University Press.

Snieder, R., & Vrijlandt, M. 2005. Constraining the Source Separation with Coda Wave Interferometry: Theory and Application to Earthquake Doublets in the Hayward Fault, California. *Journal of Geophysical Research*, **110**, 1–15.

Sparkman, G. 2002. Shallow or Deep, Which is it? *The Leading Edge*, july, 659.

Terzaghi, K., Peck, R. B., & Mesri, G. 1996. *Soil Mechanics in Engineering Practice, Third Edition*. John Wiley and Sons.

Turcotte, D. L., & Schubert, G. 2002. *Geodynamics, Second Edition*. Cambridge University Press.

Wald, D. J., Quitoriano, V., Heaton, T. H., Kanamori, H., Scrivner, C. W., & Worden, C. B. 1999. TriNet "ShakeMaps": Rapid Generation of Peak Ground Motion and Intensity Maps for Earthquakes in Southern California. *Earthquake Spectra*, **15**(3), 537–556.

APPENDIX A

DERIVATION OF STATIC STRESS EQUATIONS

Given the coordinate system defined in Figure 2.1, there is no force acting on the topographic surface, providing a traction-free boundary. This gives the boundary conditions at the surface,

$$\sigma_{zz}(z=0) = \sigma_{xz}(z=0) = 0 \; . \tag{A.1}$$

Lateral strain is defined as zero so material cannot expand in the horizontal direction throughout the infinite slope,

$$\frac{\partial U_x}{\partial x} = 0 \; . \tag{A.2}$$

The equation of motion for the stress state that balances the gravitational force is

$$\rho \ddot{u}_i = g_i - \sigma_{ij,j} \; . \tag{A.3}$$

This convention defines compressional stress as positive and extensional stress as negative. Because the properties of the slope only depend on the distance to the surface, the variation of stress in the x-direction is discarded. Equilibrium of forces is described by the stress balance equations:

$$\frac{\partial \sigma_{xz}}{\partial z} - \rho g \sin(\theta) = 0 \; , \tag{A.4}$$

$$\frac{\partial \sigma_{zz}}{\partial z} - \rho g \cos(\theta) = 0 \ . \tag{A.5}$$

For an elastic, isotropic medium, Hooke's Law is the relationship between stress and strain

$$\sigma_{ij} = \lambda \delta_{ij} \epsilon_{kk} + 2\mu \epsilon_{ij} \ , \tag{A.6}$$

where δ_{ij} is the Kronecker delta, and λ and μ are Lam*é* parameters. With all derivatives in the x-direction zero, the stress in terms of displacement is:

$$\sigma_{xx} = \lambda \frac{\partial U_z}{\partial z} \ , \tag{A.7}$$

$$\sigma_{zz} = (\lambda + 2\mu) \frac{\partial U_z}{\partial z} \ , \tag{A.8}$$

$$\sigma_{xz} = \mu \frac{\partial U_x}{\partial z} \ . \tag{A.9}$$

Since $\partial U_z / \partial z = \sigma_{xx} / \lambda$, this is inserted into (A.8):

$$\sigma_{zz} = \frac{\lambda + 2\mu}{\lambda} \sigma_{xx} \ , \tag{A.10}$$

giving,

$$\sigma_{xx} = \frac{\lambda}{\lambda + 2\mu} \sigma_{zz} \ . \tag{A.11}$$

Integrate equations (A.4-A.5) to find static stress as a function of depth:

$$\sigma_{zz} = \int \rho g \cos(\theta) dz = \rho g z \cos(\theta) + s \ , \tag{A.12}$$

$$\sigma_{xz} = \int \rho g \sin(\theta) dz = \rho g z \sin(\theta) + s \ , \tag{A.13}$$

where the constant, s, must be zero due to equation (A.1). Therefore, the static stress state is given by:

$$\sigma_{xx}^{static} = \frac{\lambda}{\lambda + 2\mu} \rho g z \cos(\theta) \ , \tag{A.14}$$

$$\sigma_{zz}^{static} = \rho g z \cos(\theta) \ , \tag{A.15}$$

$$\sigma_{xz}^{static} = \rho g z \sin(\theta) \ . \tag{A.16}$$

APPENDIX B

FAILURE OF A HORIZONTAL SLOPE

If we consider level ground at rest, a unit of soil at depth has a maximum principal stress equal to the overlying weight in the vertical direction and minimum principal stress in the horizontal direction. From elastic theory, we can describe the principal stresses in terms of Poisson's ratio:

$$\sigma_3 = \frac{\nu}{1-\nu}\sigma_1 \ , \tag{B.1}$$

$$\frac{\sigma_1}{\sigma_3} = \frac{1-\nu}{\nu} \ . \tag{B.2}$$

Assuming a cohesionless soil, Mohr-Coulomb theory states that failure occurs when:

$$\frac{\sigma_1}{\sigma_3} \geq tan^2(45 + \frac{\phi}{2}) \ , \tag{B.3}$$

$$\frac{\sigma_1}{\sigma_3} \geq \frac{1+sin(\phi)}{1-sin(\phi)} \ . \tag{B.4}$$

We can relate Poisson's ratio to failure by substituting equation (B.2):

$$\frac{1-\nu}{\nu} \geq \frac{1+sin(\phi)}{1-sin(\phi)} \ . \tag{B.5}$$

Therefore, elastic theory used in this model predicts failure of level ground if:

$$\nu \leq \frac{1}{2}(1-sin(\phi)) \ . \tag{B.6}$$

APPENDIX C

DERIVATION OF DYNAMIC STRESS EQUATIONS

Given Newton's Law and Hooke's Law:

$$-\rho\omega^2 U_x = \frac{\partial \sigma_{xx}}{\partial x} + \frac{\partial \sigma_{xz}}{\partial z} \,, \tag{C.1}$$

$$-\rho\omega^2 U_z = \frac{\partial \sigma_{xz}}{\partial x} + \frac{\partial \sigma_{zz}}{\partial z} \,, \tag{C.2}$$

$$\sigma_{xx} = (\lambda + 2\mu)\frac{\partial U_x}{\partial x} + \lambda \frac{\partial U_z}{\partial z} \,, \tag{C.3}$$

$$\sigma_{zz} = \lambda \frac{\partial U_x}{\partial x} + (\lambda + 2\mu)\frac{\partial U_z}{\partial z} \,, \tag{C.4}$$

$$\sigma_{xz} = \mu \left(\frac{\partial U_z}{\partial x} + \frac{\partial U_x}{\partial z} \right) \,. \tag{C.5}$$

At the surface, $\sigma_{zz}(z = 0) = \sigma_{xz}(z = 0) = 0$. We want to find how stress behaves near the free surface and express this in the displacement. Since the z-derivative of displacement cannot be measured, $\partial U_z/\partial z$ is eliminated from (C.3-C.4) by taking $(\lambda + 2\mu)\,(C.3) - (\lambda)(C.4)$:

$$(\lambda + 2\mu)\,\sigma_{xx} - \lambda \sigma_{zz} = \left((\lambda + 2\mu)^2 - \lambda^2 \right) \frac{\partial U_x}{\partial x} \,. \tag{C.6}$$

At the surface, $\sigma_{zz} = 0$, hence,

$$\sigma_{xx}^{(0)} = \frac{4\mu\,(\lambda + \mu)}{\lambda + 2\mu} \frac{\partial U_x}{\partial x} \,, \tag{C.7}$$

where $\sigma_{ij}^{(0)}$ refers to the stress at the surface of the slope. Using a Taylor series expansion, $\sigma_{xx}(z) = \sigma_{xx}^{0} + 0(z)$. The first term gives the dominant contribution of σ_{xx} near the surface, which is (C.7) in this approximation. Since $\sigma_{zz}^{(0)} = 0$,

$$\sigma_{zz}(z) = \frac{\partial \sigma_{zz}^{(0)}}{\partial z} z + O(z^2) \; . \tag{C.8}$$

$\partial \sigma_{zz}^{(0)} / \partial z$ is found by evaluating (C.2) at $z = 0$, where σ_{xz} vanishes at the free surface, hence

$$-\rho \omega^2 U_z^{(0)} = \frac{\partial \sigma_{zz}^{(0)}}{\partial z} \; . \tag{C.9}$$

Inserting this into (C.8) gives:

$$\sigma_{zz}(z) = -\rho \omega^2 U_z^{(0)} z + O(z^2) \; . \tag{C.10}$$

Similarly,

$$\sigma_{xz}(z) = \frac{\partial \sigma_{xz}^{(0)}}{\partial z} z + O(z^2) \; . \tag{C.11}$$

Substitute (C.7) into (C.1) to evaluate this derivative at the free surface,

$$-\rho \omega^2 U_x = \left\{ \frac{\partial}{\partial x} \left(\frac{4\mu(\lambda + \mu)}{\lambda + 2\mu} \frac{\partial U_x}{\partial x} \right) \right\} + \frac{\partial \sigma_{xz}}{\partial z} \; , \tag{C.12}$$

$$\frac{\partial \sigma_{xz}}{\partial z} = -\rho \omega^2 U_x - \left\{ \frac{\partial}{\partial x} \left(\frac{4\mu(\lambda + \mu)}{\lambda + 2\mu} \frac{\partial U_x}{\partial x} \right) \right\} \; . \tag{C.13}$$

Therefore, the dynamic stress equations for the near-surface are:

$$\sigma_{xx}^{dyneq}(z) = \frac{4\mu(\lambda + \mu)}{\lambda + 2\mu} \frac{\partial U_x^{(0)}}{\partial x} + O(z) \; , \tag{C.14}$$

$$\sigma_{zz}^{dyneq}(z) = -\rho \omega^2 U_z^{(0)} z + O(z^2) \; , \tag{C.15}$$

$$\sigma_{xz}^{dyneq}(z) = -\left\{\rho\omega^2 U_x^{(0)} + \frac{\partial}{\partial x}\left(\frac{4\mu(\lambda+\mu)}{\lambda+2\mu}\frac{\partial U_x^{(0)}}{\partial x}\right)\right\} z + O(z^2) \ . \tag{C.16}$$

For a plane wave, the displacement is given by:

$$U(x,z,t) = U(t-px,z) \ , \tag{C.17}$$

where p is the slowness or ray parameter. Therefore, the derivative of displacement is expressed as:

$$\frac{\partial U_x}{\partial x} = -p\frac{\partial U_x}{\partial t} = -pv \ , \tag{C.18}$$

where v is the particle velocity. In the frequency domain, this relationship can be written as:

$$\frac{\partial U_x}{\partial x} = \frac{-p}{-i\omega}a_x = \frac{p}{2\pi i f}a_x \ , \tag{C.19}$$

where a_x is acceleration, and f the frequency of the wave. The derivative of displacement is approximately equal to:

$$\left|\frac{\partial U_x}{\partial x}\right| \approx \left|\frac{p}{2\pi f}a_x\right| \ . \tag{C.20}$$

The slowness, p, is also related to the angle of incidence and the velocity at the surface,

$$p = \frac{sin(i_p)}{v_p} = \frac{sin(i_s)}{v_s} \ . \tag{C.21}$$

By substituting (C.20) for the derivative of displacement in equations (C.14-C.16), the stress components are related to slowness and, hence, the angle of incidence of a plane wave,

$$\sigma_{xx}^{dyneq}(z) = \frac{4\mu(\lambda+\mu)}{\lambda+2\mu}\left(\frac{p}{2\pi f}\right)a_x \ , \tag{C.22}$$

$$\sigma_{zz}^{dyneq}(z) = -\rho a_z z \ , \tag{C.23}$$

$$\sigma_{xz}^{dyneq}(z) = -\left\{ \rho a_x + \left(\frac{4\mu(\lambda+\mu)}{\lambda+2\mu} \right) \left(\frac{p}{2\pi f} \frac{\partial a_x}{\partial x} \right) \right\} z \ . \tag{C.24}$$